Accepted version (Postprint) for publication in Atmospheric Research of manuscript:

On the conditions for winter lightning at the Eagle Nest Tower (2537 m asl) during the Cerdanya-2017 field experiment

Serge Soula[a,*], Nicolau Pineda[b,c], Jean-François Georgis[a], Antoine Leroy[a], Igor Vanpoucke[a], Joan Montanyà[c], Enric Casellas[d], Sergi Gonzalez[d,e], Joan Bech[d]

[a] *Laboratoire d'Aérologie, Université de Toulouse, CNRS, Toulouse, France*
[b] *Meteorological Service of Catalonia, Barcelona, Spain*
[c] *Lightning Research Group, Technical University of Catalonia, Terrassa, Spain*
[d] *Dept. Applied Physics Meteorology, University of Barcelona, Barcelona, Spain*
[e] *DT Catalonia, Agencia Estatal de Meteorología (AEMET), Barcelona, Spain*

A B S T R A C T

In this paper, we analyze meteorological conditions, thundercloud structure, lightning activity and characteristics of the flashes that strike two towers separated by 1.3 km on Tosa d'Alp (2537 m asl) for two days (March 24 and 31) of the Cerdanya-2017 field campaign. Remote sensing products (cloud top temperature, lightning flash location, volumetric radar scans) and a set of sensors installed at Cerdanya station (electric field mill, microwave radiometer, vertically-pointing K-band Doppler radar, atmospheric soundings) provide the data for the analysis. A total of 20 flashes (72 strokes) have been detected on these towers with a large majority on March 24 (18 flashes and 66 strokes), despite of a lower convective activity in the study region. All these flashes are negative and most of them exhibit the features of upward flashes: large multiplicity (3.67 in average on March 24), strokes with low peak current (−10.6 kA in average on March 24), and short inter-stroke time interval (40 ms in average on March 24). Some flashes are supposed to be self-triggered on the towers because of the absence (the low number) of VHF sources before (after) the strokes. Compared to the instrumented "Eagle Nest Tower", the "Cerdanya Tardia Antenna" collects a greater number of flashes (strokes) during the most prolific day with 14 out of 18 (57 out of 66). During this day, all flashes that radiate in VHF at less than 5 km from the towers strike them. We observe also that the cloud region around −15 °C favorable for charging process is located at lower altitude (1000 m above tower altitude) and produce strong radar reflectivity values on that day. Furthermore, the wind at the altitude of Tosa d'Alp stronger on March 24 could facilitate the inception from the towers by evacuating the corona ions.

1. Introduction

Winter lightning only accounts for a small percentage of the annual lightning activity, which mainly concentrates in summer months in mid-latitude regions. Poelman et al. (2016) found that only 3% of the annual lightning occurs during winter in Europe, the percentage even being lower for the continental U.S. (0.03% according to Adhikari and Liu, 2019). Nevertheless, winter thunderstorms can produce very en- ergetic CG lightning events and a large amount of damage on structures at the ground (e.g. Wang and Takagi, 2012; Matsui et al., 2020).

Interest in winter lightning has grown in recent years, notably because of the global expansion of wind power generation (e.g. Leung and Yang, 2012; Mendez et al., 2018). Keeping in mind the dependence of the electrification processes on temperature (e.g. Takahashi, 1978; Saunders et al., 2006), cloud charges are at lower altitudes in winter, favoring interaction with ground structures such as wind turbines, as reported in literature (Wang and Takagi, 2012; Montanyà et al., 2014; Schultz et al., 2018; Pineda et al., 2018a; Soula et al., 2019). Consequently, the concept of winter lightning has been recently introduced and conceptualized in the 2018 revision of the "Lightning Protection of Wind Turbines" standard IEC 61400-24 (Mendez et al., 2018). Another sector that suffers from winter lightning is aviation. Lightning Initiation by aircraft can be more efficient when thundercloud charges are closer to the ground, conditions that are mainly fulfilled during wintertime (e.g. Mäkelä et al., 2013; Wilkinson et al., 2013).

Winter lightning should not only be restricted to those occurring during the winter season, but include lightning occurring under typical winter environmental conditions, which can be reached outside the winter season. In this regard, the term winter type-lightning could be more appropriate. Montanyà et al. (2016) suggested a criterion for the identification of winter-type lightning worldwide: those occurring when temperatures are equal or lower than −10 °C at the 700 hPa level. The global map of winter lightning resulting from this criterion revealed the most active areas worldwide. Apart from the well-known coastal areas of the Sea of Japan, other significant active areas during winter are the north of the Mediterranean basin (especially the Adriatic Sea region), the Great Lakes and part of the East Coast of the U.S., Uruguay and surroundings, and southern New Zealand.

* Corresponding author.
E-mail address: serge.soula@aero.obs-mip.fr (S. Soula).

https://doi.org/10.1016/j.atmosres.2020.105208

Most of winter lightning to tall structures belong to the upward lightning type. Studies like Warner et al. (2014), Jiang et al. (2014), Schultz et al. (2018), Bech et al. (2013) and Pineda et al. (2018a) have shown that enhanced electric fields at the top of tall structures, combined with a lower altitude of the charge centers (e.g. Montanyà et al., 2016) were enough to allow the initiation of upward lightning. In fact, upward lightning has also been reported on small towers located on mountain tops (e.g. Pineda et al., 2018b). The shape of the mountain appears to be adding a field enhancement factor, resulting in an "effective height" that is considerably greater than the physical height of the tower (Rizk, 1994; Zhou et al., 2010).

During a thunderstorm, the presence of space charge produced by glow corona at the tip of tall objects can hinder the triggering of lightning (Becerra et al., 2007; Bazelyan et al., 2015). However, a strong wind can remove the corona shield, thus clearing the way for initiation of an upward leader (Wang and Takagi, 2012). According to Mazur (2016) this is the most probable explanation for the upward leader inception in the absence of the preceding nearby lightning fla- shes. Wang and Takagi (2012) noted that self-initiation upward light- ning (SIUL) occurred with higher observed wind speeds (or a rotating windmill) compared with other-triggered upward flashes. On blizzard conditions in the U.S., Warner et al. (2014) suggested that notable winds may have played a key role in SIUL, by "stripping" away much of the corona discharge shielding grounded tall structures. On the other hand, the effect of blades rotation on wind turbines may have a similar effect, enhancing lightning inception from wind turbines (Rachidi et al., 2008; Montanyà et al., 2014).

This study focuses on a comparison of two storm events that occurred on March 2017 during the campaign Cerdanya-2017 in Northeastern Spain. In the campaign area in the Spanish Pyrenees mountain range there is an instrumented station and a mountain peak with two high structures. The two storm cases exhibit specific meteorological conditions and strongly different behaviors in terms of number of lightning strikes on the ground structures, so the study can contribute to shed new light on the specific meteorological conditions favoring winter lightning. The organization of the paper includes Section 2 that describes the context of this campaign, the site of instrumentation and the different data used in the study, Section 3 that presents the results from the observations for both events, Section 4 that provides interpretation and discussion issued from the analysis of the observations, and Section 5 that summarizes the main points of the study.

2. The Cerdanya-2017 field experiment

2.1. Objectives and site description

The field experiment Cerdanya-2017 took place from October 2016 to April 2017, in the Spanish part of the Cerdanya valley, thanks to the joint effort of several teams from the Euroregion Pyrenees-Mediterranean. These teams belong to the Universities of the Balearic Islands and of Barcelona, METEO-FRANCE, CNRS, University of Toulouse and the Meteorological Service of Catalonia. The Cerdanya basin sits around 1000 m above sea level (asl) in the Eastern Pyrenees. Unlike most of the Pyrenean valleys, it is oriented from ENE to WSW, nearly parallel to the mountain ranges (Fig. 1). The main measurement site of the Cerdanya-2017 field campaign was deployed at the centre of the basin, in the Cerdanya Aerodrome (Fig. 1).

The experiment focused on three meteorological phenomena in mountainous terrain: cold pool, mountain waves and orographic processes. In particular, it analyzed the detailed inversion structure and the surface energy budget of cold pool (Conangla et al., 2018), rotors and boundary layer separation in mountain wave situations (Udina et al., 2020), and orographic triggering and intensification of precipitations under stratiform and convective regimes (Gonzalez et al., 2019). In parallel to these research topics and taking advantage from both measurements made on the campaign site and remote sensing products, the present study on electrical characteristics of some meteorological events could be developed.

2.2. The instrumentation

During the long-term campaign covering 7 months, several automatic measuring equipments were used to study kinematic and thermodynamic characteristics of the atmosphere. The site for the ground observations was located on the aerodrome of Cerdanya (1.867°E; 42.387°N; 1100 m asl) and called Cerdanya Station (CS, hereafter). A Humidity And Temperature microwave PROfiler (HATPRO, Rose et al., 2005) was installed to retrieve profiles of temperature and humidity up to 3 km altitude and to perform fast Liquid Water Path (LWP) sampling, i.e. the total amount of liquid water present up to 3 km altitude, with a 1-s time resolution. This ground-based microwave radiometer detects thermal emission of the atmosphere at 14 frequencies distributed over two bands: K-band (between 22 and 31 GHz) and V-band (between 51 and 58 GHz). The oxygen specific absorption features around 60 GHz (in the V-band) and the water vapor absorption line around 22.235 GHz (in the K-band) are used to derive information about their abundance and vertical structure. Since liquid water emission increases with frequency, the brightness temperatures measured in the K-band around 31 GHz are dominated by liquid absorption and then provide supplementary information on the columnar amount of liquid water. The temperature profile in the atmosphere is directly derived from the brightness temperature measured along the oxygen absorption complex (in the V-band) and the well-known vertical profile of oxygen concentration since the emission at any altitude is proportional to local temperature and oxygen density. The amount of the integrated water vapor, the liquid water path as well as the atmospheric temperature and specific humidity profiles are all retrieved from a statistical inversion methodology (Löhnert and Crewell, 2003).

On the other hand, a Micro Rain Radar (MRR) provided precipitation vertical profile observations. The MRR is a Doppler radar vertical profiler operating at 24 GHz (Peters et al., 2005, 2010) and was configured to derive 1-min averaged vertical profiles of 3 km above ground level estimates of equivalent radar reflectivity (hereafter radar reflectivity), spectral width and Doppler vertical velocity at 100 m resolution. Although MRR was first developed to observe liquid precipitation and has been widely used for this purpose (e.g. Bendix et al., 2006; Adirosi et al., 2016) its application to snow observation has also been demonstrated (e.g. Kneifel et al., 2011; Garrett et al., 2015). MRR has been recently applied to solid precipitation studies (Stark et al., 2013; Souverijns et al., 2017; Gonzalez et al., 2019). Data was post-processed using the methodology proposed by Maahn and Kollias (2012) which is especially suited for winter precipitations. One of the important uses of the MRR is the detection of the melting layer, based on the conventional "bright band" signature. The bright band (BB) is a thin, rather horizontal layer of enhanced radar reflectivity resulting primarily from the fast increase in the dielectric constant of particles during the melting process and sharp gradient of fall speeds of precipitation particle (e.g. White et al., 2002; Massmann et al., 2017).

The electric field measurement is performed by a fieldmill of Previstorm type from Ingesco Company described in Montanyà et al. (2009) and used during previous campaigns in France (Soula et al., 2003; Soula and Georgis, 2013). This sensor has a downward electrode within the measurement head that avoids rain disturbances. In the field of experiment the sensor is mounted on a 1-m mast installed on flat terrain. The geometry of this installation reverses and reinforces the electrostatic field on the electrode. Before its use during the experimental campaign, the sensor was tuned so that its analogical signal was fixed to zero when the electrode was completely shielded by a conductive mask. Then, during the measurement analysis, several days of fair weather were used to determine an average value of the electrostatic field provided by the sensor in these conditions. By considering

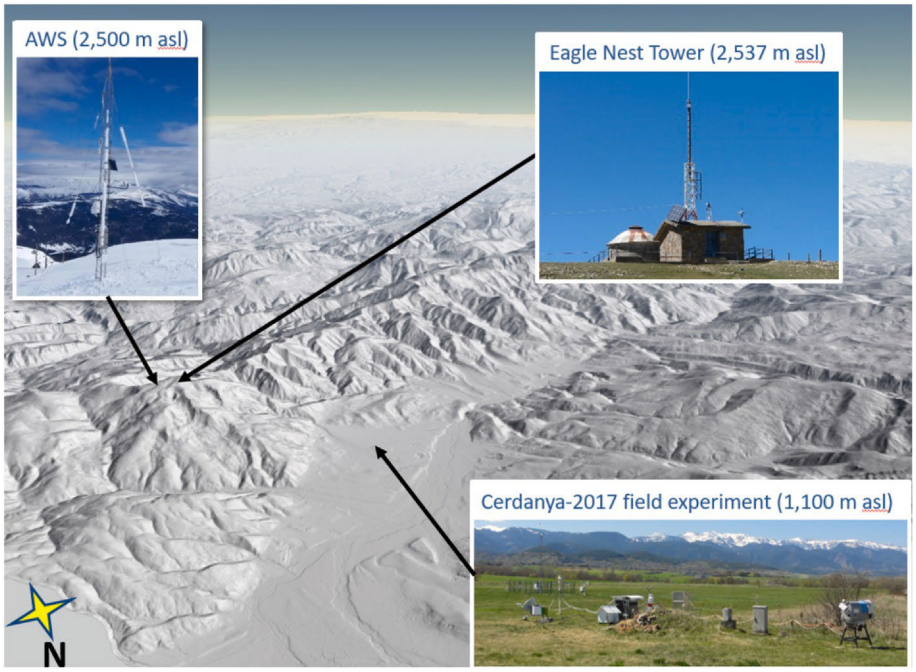

Fig. 1. The Cerdanya valley, located in the Eastern Pyrenees mountain range, oriented ENE-WSW across Spain and France, 10 km wide and 35 km long. The pictures superimposed show the Tosa d'Alp Automatic Weather Station (2500 m asl), the Eagle Nest Tower 25 m high, and the field experiment Cerdanya-2017 located at the Aerodrome of Cerdanya (1100 m asl) with the MRR, the HADPRO radiometer and the electric field mill.

that the fair-weather electrostatic field value is close to 130 V m^{-1}, the coefficient due to the geometry of the sensor with its support can be calculated and used to correct the values provided during the atmospheric events documented. The extreme values reported during the campaign and corresponding with the saturation were − 11.4 kV/m and 11.4 kV/m, for negative and positive polarity, respectively. However, these extreme values were very rarely reported, only after a rapid variation due to a lightning flash during one or two seconds. The data from this sensor has been recorded with a time resolution of 1 s. This time resolution reveals the major discontinuities in the electrostatic field caused by the lightning flashes without the distracting effects of much faster individual processes within a flash. The polarity of the field is considered as positive when it is created by negative charge overhead. In practice, the polarity of the field provides an indication of the most efficient charge above ground and its evolution can indicate either a modification of the values of the charges within the thunderstorm or their displacement. It is therefore difficult to discuss the location and the polarity of the charge to interpret the electrostatic field recordings. The Eagle Nest Tower (hereafter, ENT) is located on Tosa d'Alp (2537 m asl) summit in the eastern part of the Pyrenees (Fig. 1). It is one of the few instrumented towers around Europe (along with Gaisberg in Austria, Säntis in Switzerland and Peissenberg in Germany). Since 2011, the tower is instrumented to measure direct lightning strikes, see details in Pineda et al. (2018b). It is worth noticing that the ENT is a peculiar installation, since it is the smallest of the instrumented towers around the world (25 m), but, at the same time, the one at the highest peak (2537 m asl) (Fig. 1).

2.3. Remote sensing products

2.3.1. Lightning detection

The lightning flash activity is continuously monitored within the studied area thanks to two lightning location systems (LLS). First, as in many previous studies (Soula et al., 2019), we use data from the network operated by Météorage French company (hereafter, Météorage). This LLS is part of the EUropean Cooperation for LIghtning Detection (EUCLID), collaboration among national lightning detection networks with the aim to detect and localize lightning all over Europe (Poelman et al., 2016). It records characteristics such as the location, polarity, peak current, and the occurrence times of strokes for CG flashes and for a part of IC flashes. The sensors of the LLS detect the magnetic field radiated in Low Frequency (LF) range thanks to double crossed frames. Both magnetic directions finding (MDF) and time of arrival (TOA) techniques allow determining the location of the strokes with good detection efficiency (DE) for CG flashes (Poelman et al., 2016). DE is for example around 90% for negative CG (CG-) strokes and the location accuracy is better than 100 m for 50% of strokes (Schulz et al., 2016). CG and IC strokes are grouped in flashes thanks to temporal and spatial criteria of ~0.5 s and ~ 10 km (Soula et al., 2019). However, both individual strokes and CG flashes are used indistinctly in the present study.

Second, the LLS operated by the Meteorological Service of Catalonia (SMC) allows monitoring total lightning (IC + CG) activity in Catalonia (north-eastern Spain) (Pineda and Montanyà, 2009). This LLS (hereafter, XDDE) is composed of four VAISALA LS8000 and one TLS200 interferometric stations that operate as a very high frequency (VHF) interferometer at ~110–118 MHz. IC flashes are located using interferometry technique (Lojou et al., 2009). The combination of the four different concurrent observations provides two-dimensional location of the IC sources, as the baseline of the XDDE does not allow three-dimensional location. Each station (LS8000 or TLS200) is also equipped with a low frequency (LF) sensor to detect and locate the return strokes by using TOA/MDF technique, which enables discrimination between IC and CG flashes. The DE for CG flashes estimated from previous campaigns is ~80% for the domain considered in the present study (Pineda and Montanyà, 2009).

2.3.2. Cloud structure and characteristics

Weather radar data are used here to determine thunderstorm characteristics. The SMC operates a weather radar network in the region, which consists of four C-band (5.600 to 5.650 MHz) Doppler radars. Polar volumes are acquired every 6 min, through a fourteen-elevation scan scheme. From this volumetric data, operative products like the Constant Altitude Plan Position Indicator (CAPPI, i.e. Fig. 3d–f) are produced every 6 min. Volumetric data allows also to examine vertical cross sections on the reflectivity field (i.e. Fig. 3g–i). Further technical details of the SMC weather radar and network characteristics can be found in Argemí et al. (2014). Despite radar beam blockage in the Pyrenees area may be a problem (see Bech et al., 2003 or Trapero et al., 2009 for details), note that most echoes of the analyzed radar data are

south of the Pyrenees range, well covered by the SMC weather radar network.

To analyze Cloud Top Temperatures (CTT), we use data from the Spinning Enhanced Visible and Infrared Imager (SEVIRI) onboard the Meteosat Second Generation (MSG) satellite launched and operated by the European Space Agency (ESA) and the European Organization for the Exploitation of Meteorological Satellites (EUMETSAT), respectively. SEVIRI is a radiometer that scans the Earth disk to provide images in 12 spectral bands every 15 min at a spatial resolution of 0.027°, which corresponds to 3 km at nadir, below the geostationary satellite located at 0° longitude on the equator. The CTT is provided by the thermal infrared band (IR) at ~11–13 μm. The temperature accuracy is generally better than ~1 °C. We consider the parallax error for the latitude region (estimated to be about 15 km for a cloud top at ~12 km at this latitude) for the figures that associate the locations of CG strokes with their parent clouds.

3. Results

3.1. Case of 24 March

3.1.1. Overview

On 24th and 25th March 2017, a surface low to the East of Catalonia favoured an advection of moist and mild air from the Mediterranean Sea below a cut-off low at 500 hPa over the Iberian Peninsula with a cold core of −33 °C. The passage of a backward warm front from northeast to southwest resulted in a heavy snow event in the Pyrenees. Stations close to ENT site recorded 17.2 to 55.9 mm of daily pre- cipitation with 0.4 mm/min maximum rainfall rate. Fig. 2a shows evidence of lightning activity in a 160 km × 160 km region including CS and ENT on 24th March 2017. Indeed, the CG stroke density is substantial in a band in the southern part of this area, and locally in some spots scattered in the whole area with especially large values at the ENT location with a maximum value of 1.5 stroke km^{-2} according to the Météorage network. This density is calculated with a spatial re- solution of 0.05° which roughly corresponds to 5 km. Thus, the CG stroke density brings out a very active spot at the ENT location.

Fig. 2b–d displays three graphs with several parameters related to CS measurements in a subset of the event (from 20:00 to 24:00 UTC on March 24), after a warm front crossed the area of study. The vertical profile of MRR in Fig. 2b shows pulses of enhanced reflectivity as short as 5–10 min. These cells are associated with well-defined vertical cores of maximum reflectivity higher than 30 dBZ. The increased downward vertical velocity (Fig. 2c) below the 0 °C isotherm suggests the top of the melting layer (2100 m asl). It is to be noted large reflectivity values (up to 30 dBZ) observed at higher altitudes (above the 0 °C isotherm) during these events. Hydrometeor fall speed doppler spectral width values above 1.5 m s^{-1} (Fig. 2d) and downward particle velocities up to 5 m s^{-1} provide evidence of riming by colliding with supercooled droplets, ice particles can increase in mass and give birth to graupel that fall at higher speeds than ice crystals and snowflakes. From 20:30 UTC the 0 °C isotherm is slightly shifted to higher levels. This could be due either from the effect of latent heat release due to condensation of water vapor associated with positively buoyant air, or to precipitation scattering and emission as reported by Knupp et al. (2009). The first possibility would be supported by the facts that the 0 °C isotherm ascent starts around 20:40 UTC and does not change significantly when radar reflectivity increases; similarly, the −10 °C isotherm climb starts before 21:00 UTC with a time lag in respect of the 0 °C isotherm ascent.

Fig. 2c displays also electrical parameters, especially the electric field at CS and the distance of CG strokes detected by Météorage. The electric field varies with a great number of excursions in positive and negative values, with extreme values at about 7 kV/m and -10 kV/m in positive and negative polarity, respectively. The negative large values occur with flash discontinuities, especially between 21:00 and 21:30 UTC. This period corresponds to the pass of the most vigorous cells of this case study characterized by highest MRR reflectivity values and strongest vertical development (Fig. 2b), which confirms the probable presence of graupel favorable to the charging processes (Saunders et al., 1991). This period experiences also an accumulation of close strokes with a minimum distance around 8 km. This distance corresponds to that between ENT and CS and concerns the large number of strokes detected at ENT location by Météorage (Fig. 2a). The CS region was affected by new cells between 21:45 and 23:30 UTC, especially between 22:00 and 22:30 UTC, but these cells are less vigorous. The electrical activity shows that there are much less strokes detected nearby and less large electric field changes in negative polarity during this second period.

3.1.2. Storm structure analysis

Fig. 3 displays several graphs for the 20:30–21:30 UTC period and the study area: (a–c) the CTT from Meteosat radiometer with superimposed CG strokes detected by Météorage during 15 min; (d–f) the CAPPI radar reflectivity at 1 km altitude with the CG strokes detected by Météorage during 6 min; (g–i) the cross section of reflectivity along the segment plotted in the CAPPI at the same time with the CG strokes at less than 5 km and during 6 min. This 1-h period corresponds to the most active in terms of electrical activity, i.e. the higher electric field values and variations, and the number of strokes detected close to CS and ENT region. At the beginning of the period (Fig. 3a), the CTT values close to the ENT are around −60 °C while the colder ones appear in the southwestern part of the area and move northwestwards in the following tens of minutes (Fig. 3b–c). The strokes are essentially located close to the cold cores of the system for the negative ones (pink circles) and more in their periphery for the positive ones (red plus). A great number of negative strokes gather on the ENT at each step, which explains the recurrent 8-km distance for strokes in Fig. 2c. Fig. 3d–f (1-km high CAPPIs) show several bands of precipitation (30–40 dBZ) at low altitude roughly southeast-north-west oriented, reaching the ENT. Vertical cross sections (Fig. 3g–i) show the moderate development of these bands, rather reaching 5 km height. All the strokes detected during 6 min at 5 km from either side of the line are plotted in Fig. 3g–i.

Fig. 3j–o shows the same kind of plots for the period around 22:00 UTC when new cells pass over CS. The cells at that time have also large reflectivity radar values below 3000 m as indicated in Fig. 2b–c. However, much less strokes were detected close to CS and ENT. The CTT values close to the CS are not very cold, since they are around −55 °C and −50 °C at 21:55 and 22:10 UTC, respectively (Fig. 3j–k). The radar reflectivity is also much lower than 1 h before close to CS, with values lower than 20 dBZ above CS and around 25 dBZ at 22:10 UTC above ENT (Fig. 3l–m). The corresponding cross sections confirm a lower development (Fig. 3n–o).

3.2. Case of 31 March 2017

3.2.1. Overview

From March 31 to April 1 a cold front associated to an Atlantic low located in Scotland moves eastwards producing scattered showers over Catalonia that hardly accumulated 10 mm of precipitation. As shown in Fig. 4a, lightning activity was recorded during that day in the study area, with spots of stroke density spread out on a southwest-northeast-oriented band. The maximum of density is close to 0.5 stroke km^{-2} from Météorage. The edge of the last spot of stroke density is in the surroundings of ENT, with low values of about 0.1 flash km^{-2}.

Fig. 4b–d shows the convective activity recorded by the MRR at CS from 18:30 till 20:00 UTC. During this period the convective cells occur in pulses with a higher frequency and higher maximum reflectivity values (> 35 dBZ). Except at the beginning of precipitation, the strongest reflectivity values are mainly observed below 1 km altitude. MRR Doppler vertical velocity profiles show a strong velocity gradient (particle fall speed increase) due to the melting of ice crystals to rain, allowing to identify the melting layer during the middle and last steps

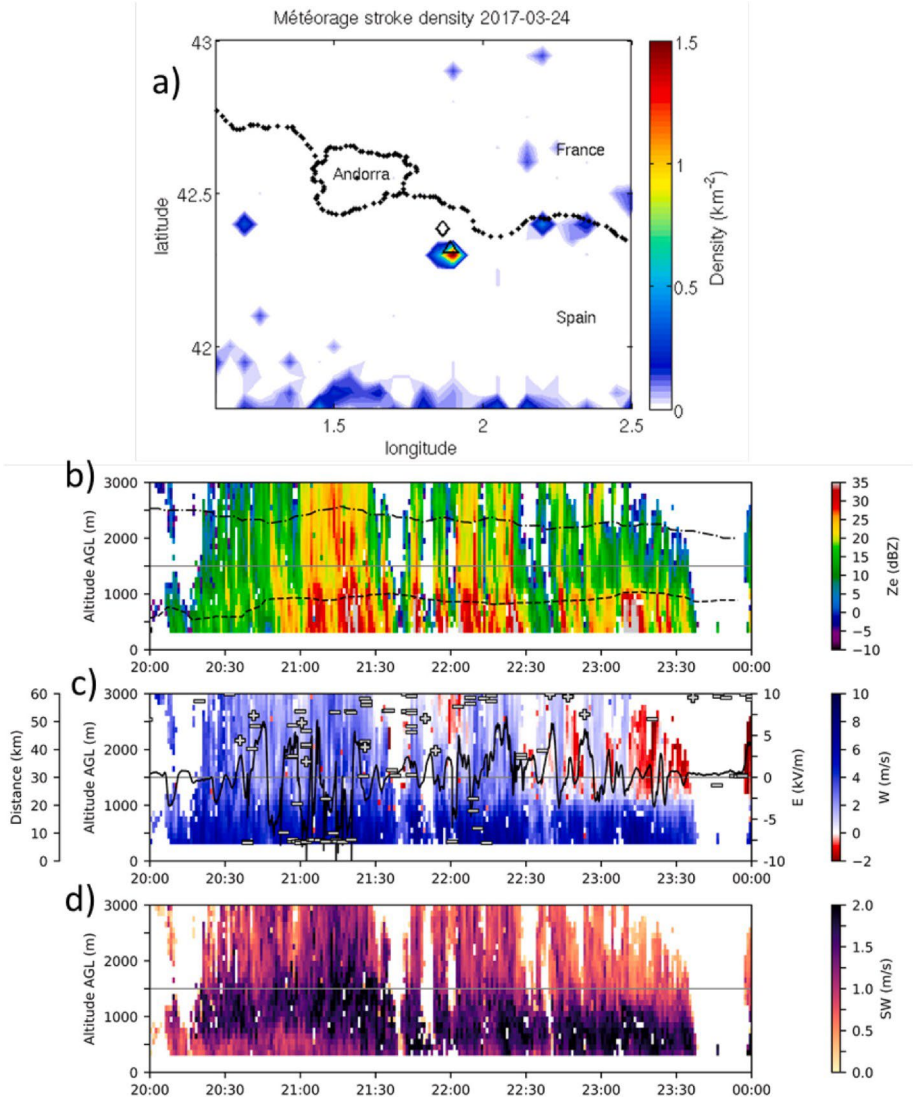

Fig. 2. Parameters measured during the storm event on March 24: a) CG lightning flash density in the region of the Cerdanya-2017 experiment calculated with a resolution of 0.05° × 0.05°, from Météorage. b) Time series of the vertical profile of the radar reflectivity, the 0 °C isotherm (dashed line) and the −10 °C isotherm (dash-dotted line). c) Time series of the electrostatic field (solid line), the distance of the CG strokes (− for CG- and + for CG+), the profile of the Doppler velocity of the falling meteors re- trieved by the radar (coloured scale). d) Time series of the profile of the spectral width retrieved by the radar. The altitude is considered above ground level (agl).

of the event (not present during the convective precipitation). The 0 °C isotherm is at about 1.3 km agl altitude before the precipitation event and rises up to 1.8 km during precipitation, and the −10 °C isotherm follows a similar pattern. As discussed in the previous case study, this effect may be due to the latent heat release due to condensation, convection, or to liquid thermal emission of precipitation (Knupp et al., 2009). On the other hand, ENT is below the freezing level from 18:00 UTC so precipitation at that level will likely be formed by solid precipitation particles and supercooled droplets, predominantly found at temperatures ranging from 0 °C to −20 °C. The precipitation profile below that level displays characteristics typical of ice-initiated rain affected by seeder-feeder process and low-level orographic precipitation enhancement including collision and coalescence among water drops (Rutledge and Hobbs, 1983; Trapero et al., 2013; Massmann et al., 2017).

The relatively strong reflectivity values observed in association with downdrafts at high altitudes are probably due to higher speeds of hydrometeor particles associated to the enhanced turbulence produced in the beginning of the event as suggested by the MRR spectral width (Fig. 4d). Fig. 4c displays also electrical parameters related to CS, i.e. the electric field locally measured, and the distance of CG lightning strokes detected by Météorage. The electric field starts to change its polarity to positive about 20 min before 18:00 UTC, then it increases during a few minutes up to 2 kV/m before a substantial decrease during a few tens of minutes around 18:00 UTC. At that moment, the MRR detects reflectivities about 20 dBZ only above an altitude of 2 km and progressively at lower altitude (Fig. 4b). This first 30-min field variation reports on the approach of a typical storm with a dipole and a positively charged anvil, and several lightning strokes detected at distances greater than 15 km from CS. When the precipitation reaches the ground at 18:20 UTC, the electric field increases rapidly up to 7.5 kV/m, which means the presence of negative charge above CS. The field decreases immediately and during 10 min as the precipitation reaches the ground around 18:30 UTC, which can be interpreted as the evacuation of negative charge by the rain to the ground (Soula et al., 2003). Simultaneously, CG lightning strokes are detected closer and closer, which confirms the storm is above the CS. During a few tens of minutes from 18:30 to about 18:50 UTC, the electric field describes large changes because of close lightning strokes and charge transfers by the rainfall. After 19:00 UTC, the electric field is much quieter and only two positive lightning strokes are detected in the surrounding area, typical observations during the end of storm. The last rain showers detected at low altitude above the CS by the MRR after 19:10 UTC (Fig. 4c) do not seem electrically charged.

3.2.2. *Storm structure analysis*

Fig. 5 shows the same parameters as Fig. 3. First, at 18:10 UTC a small cloud system approaches CS at less than 15 km, with two

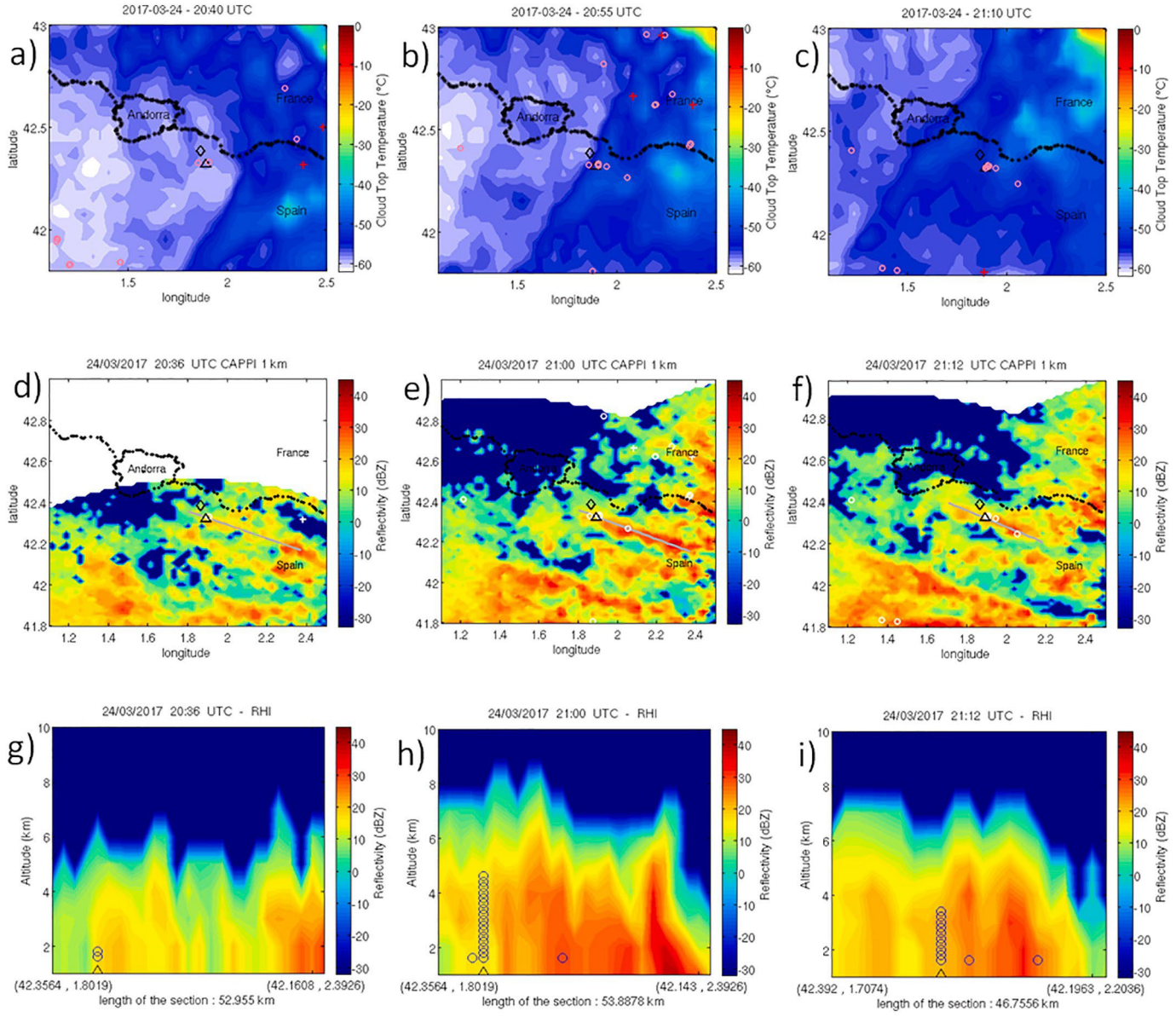

Fig. 3. Storm event on March 24: a), b) and c) CTT distribution and lightning stroke location (red plus for CG+ and pink circle for CG-) detected by Météorage during 15 min around the time of the Meteosat scanning at 20:40, 20:55 and 21:10 UTC, respectively. The triangle and the diamond indicate the locations of the tower and the station, respectively. d), e) and f) Radar reflectivity (CAPPI at 1 km) in the same area and lightning stroke location (white plus and circle for CG+ and CG-, respectively) detected by Météorage during 6 min around the time of the radar scan. g), h) and i) Radar reflectivity vertical cross section corresponding to the segment in d), e) and f), respectively. The circles correspond with lightning strokes located at less than 5 km from the segment. Following, for the same day and at 21:55 and 22:10 UTC for CTT (j,k), at 21:54 and 22:12 UTC for radar reflectivity (l–o).

apparent cells from the CTT displayed in Fig. 5a, each one producing a small number of CG flashes. The minimum CTT values are about −55 °C in both. Another cloud system at 50 km southwest to CS is more active in CG flash production and with colder CTT values (up to −60 °C). Then, at 18:25 UTC one of the cells in the closest cloud structure reaches the CS site with CTT values of about −56 °C above CS and low activity, while the second located at about 25 km southwest of CS becomes much more active with CTT at −63 °C (Fig. 5b). The other structure approaches at southwest of the first one, with less cold CTT and reduced activity. Both structures produce CG lightning strokes, essentially negative, and merge 15 min later (Fig. 5c). The core of the coldest CTT passes very close south to CS (at less than 10 km) and just above ENT. Most of CG strokes detected by Météorage concentrate in the cold core of this convective system.

The 18:12, 18:30 and 18:42 UTC radar CAPPIs (Fig. 5d–f) show a strong convective activity successively associated with both cloud systems observed from the CTT in the previous panels of the figure. Indeed, the radar reflectivity is greater than 45 dBZ at 18:12 UTC in the most southwestern system that is active earlier, while it is maximum around 40 dBZ 18 min later in the merged system south to the CS. From these three panels, the higher the reflectivity the greater number of CG strokes. Fig. 5g–i confirms the higher reflectivity at low altitude at 18:12 UTC, a stronger vertical development at 18:30 and 18:42 UTC when the system is south to CS, and lightning strokes associated with a core of reflectivity in altitude at each step of time.

3.3. *Flash characteristics*

A large amount of CG- strokes have been recorded in a 6 km × 6 km region encompassing Tosa d'Alp shown in Fig. 6, in blue on March 24 and in red on March 31. Both IC and CG strokes are included, because we consider that some events can be misclassified. Indeed, ICs may be

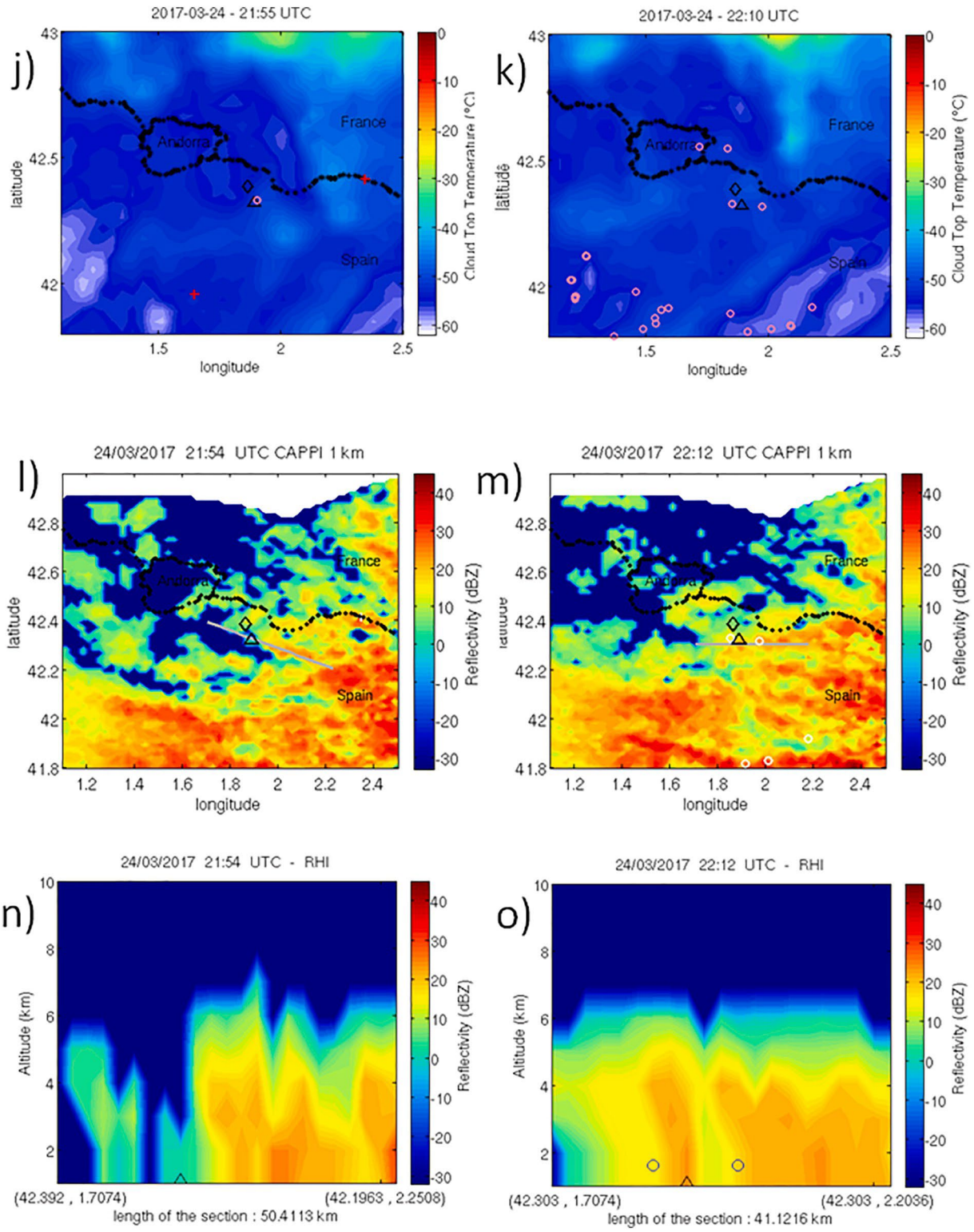

Fig. 3. (*continued*)

classified as CGs, and vice versa (Cummins and Murphy, 2009). Furthermore, several studies reported a higher rate of misidentification on LLS measurements related to towers (e.g. Warner et al., 2014; Azadifar et al., 2016; Pineda et al., 2019). They related the misclassification to the electric fields radiated from return strokes on tall towers, which have a shorter peak-to-zero time compared to regular downward fla- shes. We can see in Fig. 6 the grouping of most strokes in two locations in the area, each with a high structure, one corresponding with the tower at ENT (1.893°E; 42.320°N) and the other corresponding with Cerdanya Tardia Antenna (1.905°E; 42.331°N; 2316 m asl) called hereafter CTA. Indeed, 12 CG- strokes are concentrated at less than 500 m from ENT while 60 are concentrated at less than 500 m from CTA, and a small ten others are scattered at a larger distance. A total of 20 flashes correspond to these strokes, 18 flashes on March 24 and only 2 on March 31. The other 11 strokes scattered in the area belong also to these flashes, except one (1.883°E; 42.324°N) that belongs to one flash

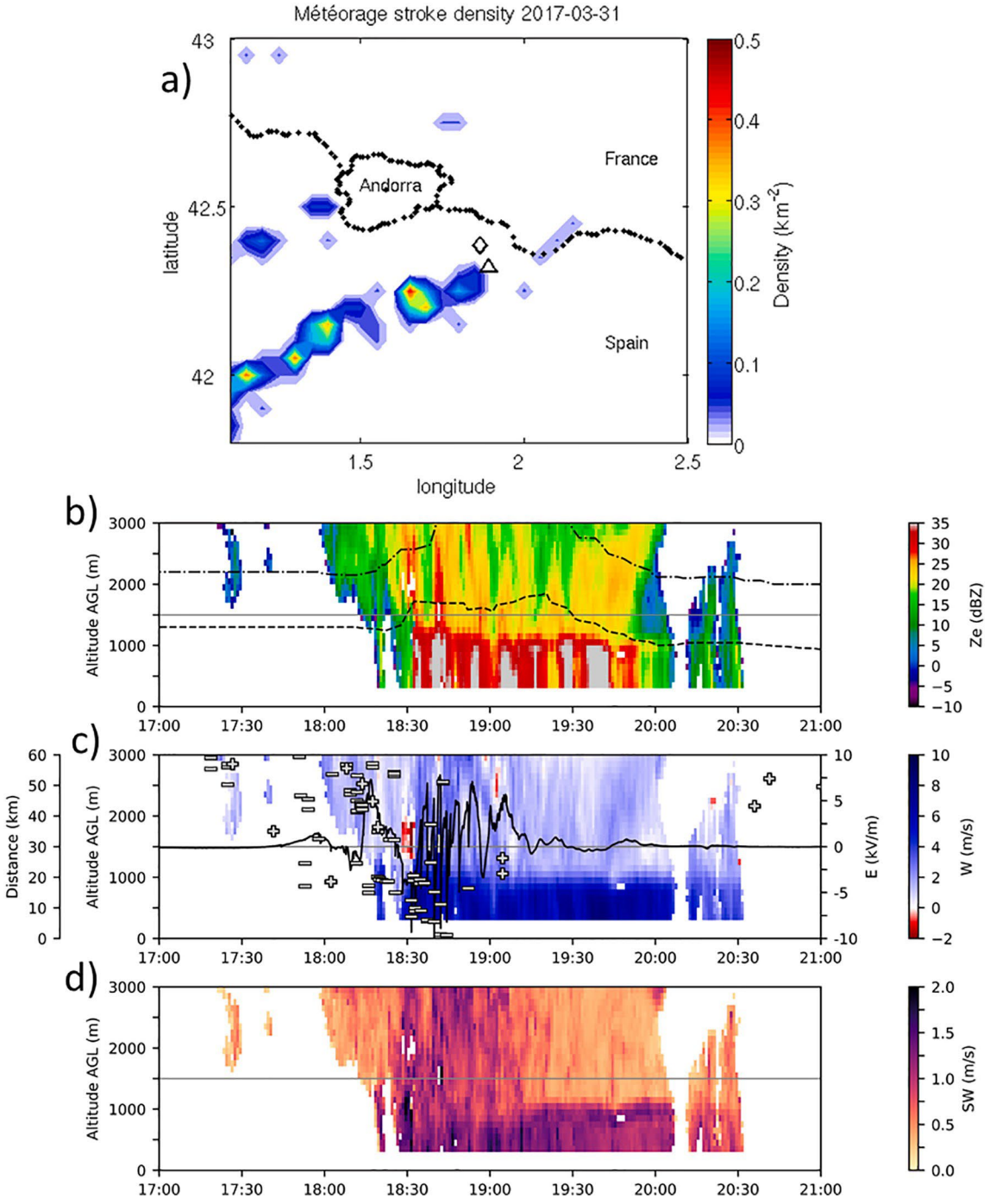

Fig. 4. Same as Fig. 2 for the storm event on March 31.

that did not have a stroke at less than 500 m from one of both tall structures.

The characteristics of all these 20 flashes are summarized in Table 1. On March 24, Météorage recorded 66 strokes from 18 flashes striking both structures, which provides an average multiplicity of 3.67. This value is large in comparison with the value of 2.80 from other flashes detected in Catalonia on that day. A large majority of the flashes strike CTA (14 out of 18) and the larger values of multiplicity correspond with these flashes, with a maximum of 11 for one flash. All strokes are negative, with an average peak current $\overline{Ip,2}$ of −10.6 kA (averaged over all 66 strokes) and a median of −8.5 kA. The average peak current $\overline{Ip,2}$ for all strokes detected by Météorage in Catalonia during the same day is substantially larger (−20.3 kA). The inter-stroke time interval has an average of 40 ms (calculated over all strokes from flashes with $M > 1$) and a median of 22 ms. The first detection for a flash can be a CG- stroke or a VHF source called IC in Table 1, and the flashes with a large multiplicity have tendency to start with a CG- stroke (seventh column in Table 1). Each flash produces a field jump detected by the field mill located to 8 km from the ENT, the values of which range between −0.5 and −12 kV/m.

Features from March 31 are very different, with only two flashes and six strokes, one that strikes ENT and one that strikes CTA. Their characteristics of peak current are closer to those of the CG- flashes detected during the day over Catalonia. Indeed, the average (median) peak current is −11.9 kA (−8.4 kA) and it is −12.6 kA for the day in Catalonia. Their average multiplicity is 3 for the flashes that strike the

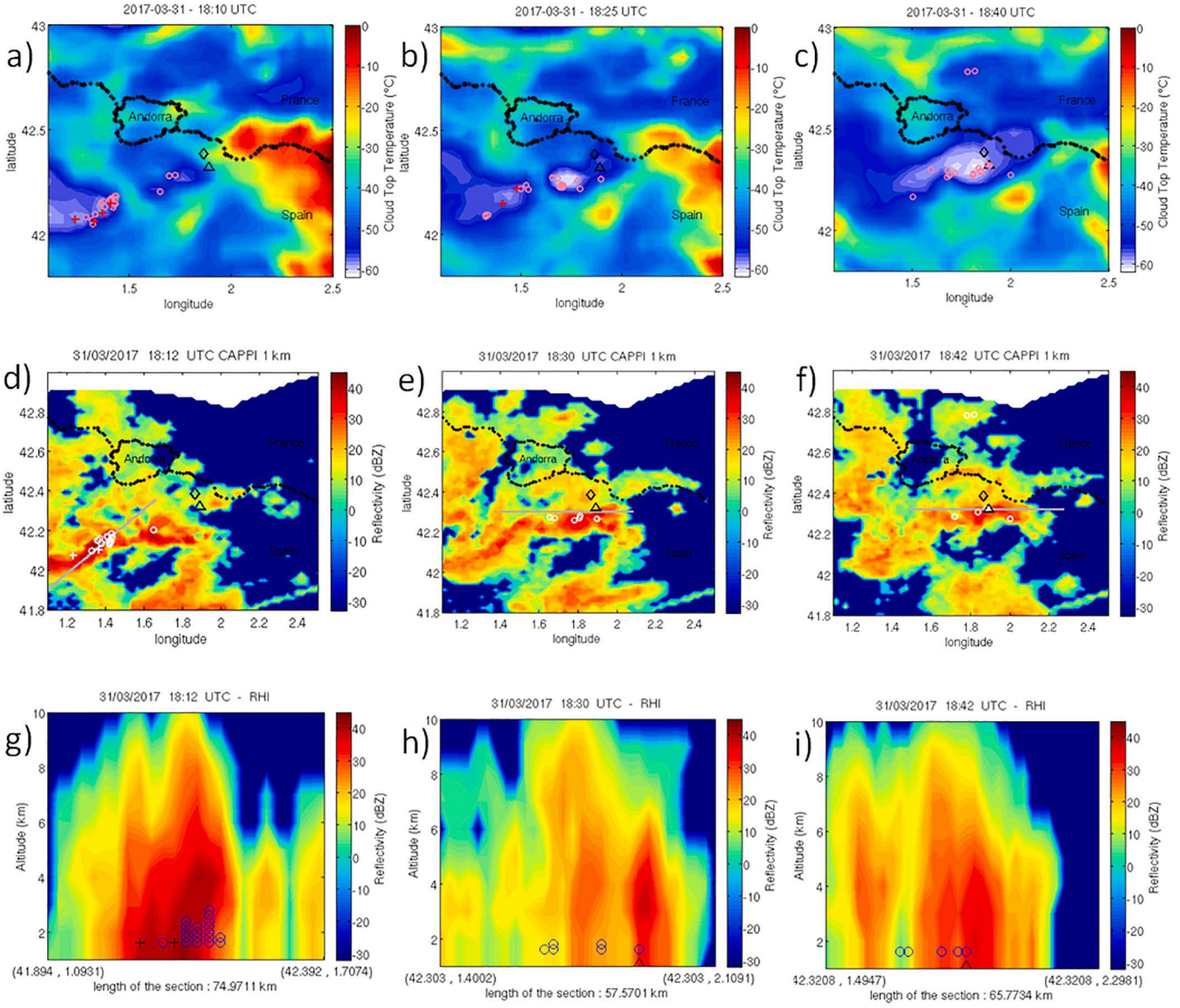

Fig. 5. Same as Fig. 3 for the storm event on March 31.

antenna and the tower, much larger than for the flashes detected along the day in Catalonia. The inter-stroke time intervals are much longer for that day with an average of 194 ms. SMC-LLS detected VHF IC sources after the Meteorage strokes at ENT and CTA, which suggests upward lightning type.

Fig. 7 displays six flashes that struck a tall structure on March 24, with CG stroke location from Météorage and VHF sources from the XDDE system superimposed with the radar reflectivity at 1 km altitude. Different cases of flashes are selected, at different periods of the storm activity, with a CG- stroke as first detected process (b,d,e), with a VHF source as first detected process (a,c,f), with strokes on ENT or on CTA (all), and with a large ΔE value detected by the field mill at CS (a,c,e,f). The first case at 20:57:01 UTC (a) shows that despite a first detection and a propagation of the flash relatively far from ENT (> 10 km), strokes can strike the antenna and produce a substantial field variation at CS (−6.9 kV/m). For the second case at 21:02:16 UTC (b) with 9 strokes on CTA, VHF sources very close to CS and ENT, and a field variation measured on the field mill of only −5.5 kV/m, the first de- tection is a CG- stroke. The third case at 21:04:31 UTC (c) is a case with a large field variation (−12 kV/m) for which the first detection is a VHF source located east of ENT and propagates westwards to both ENT and CS with 4 strokes detected on ENT. The fourth case at 21:10:04 UTC (d) produces a great number of CG- strokes on CTA including the first detection, a propagation on a short distance and a low field variation at CS (−5.2 kV/m). For the fifth case at 21:16:42 UTC (e), a CG- stroke was first detected on CTA. Then, 3 other CG- strokes struck CTA, only a few VHF sources were detected, and a field variation of −8.2 kV/m was measured at CS. The last case at 22:00:04 UTC (f) produced VHF sources detected at more than 20 km from CTA and propagates progressively toward CTA to strike it three times.

Fig. 8 displays in the same way four flashes for March 31, all in the area of ENT and CTA but only two striking them (c,d) and reported in Table 1. Fig. 8a displays a flash at 18:31:29 UTC with a first detection of VHF sources in the area with large reflectivity values around 40 dBZ. The flash propagates over a long distance across the convective line (~50 km) with a great number of VHF detections (183) and strikes the ground (CG-) at two locations, one of which at a few kilometers from ENT. It produces VHF sources located above ENT, but no stroke is detected on it. The field mill at CS detects a substantial ΔE with a value of −6.4 kV/m, suggesting neutralization of negative charge within the cloud at low distance. The flash at 18:42:09 UTC in Fig. 8b is first detected with a CG- stroke very close to ENT (about 1 km west of ENT,

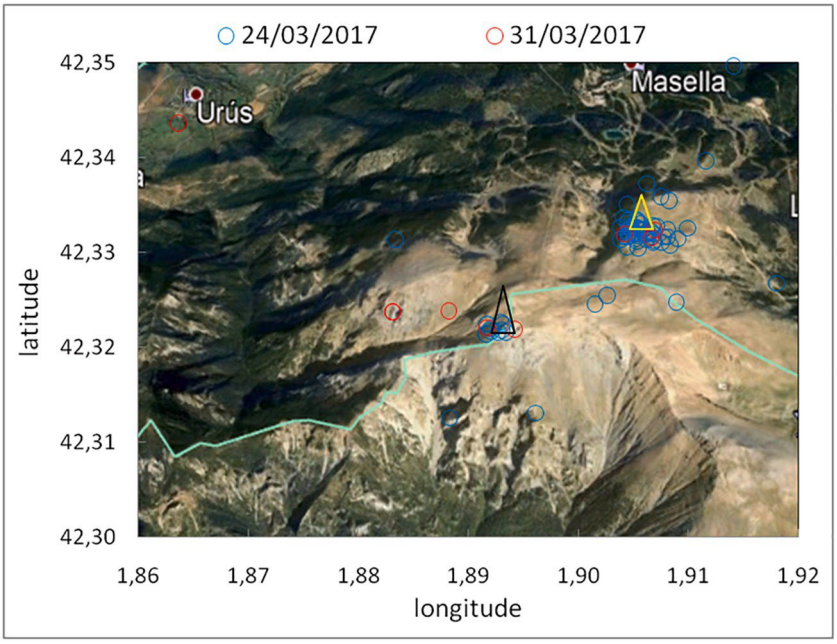

Fig. 6. Zoom on the region of the ENT with the location of the CG- strokes detected by Météorage, blue circles for March 24 and red circles for March 31. The black and yellow triangles indicate the location of ENT and CTA, respectively.

also visible in Fig. 6) that produces a very strong peak current (−96.5 kA) and is followed by a high density of VHF sources around. This flash lowers a large amount of negative charge to the ground because it produces a very large ΔE of −15.5 kV/m at CS. The flash at 18:44:19 UTC in Fig. 8c produces VHF sources first detected 5 km north of ENT and strikes it three times about 400 milliseconds later. It produces a very large ΔE values at CS, −11.8 kV/m, which indicates that the ne- gative charge neutralized is very close or/and large. The last flash in Fig. 8d at 18:48:49 UTC strikes CTA three times and produces a few VHF sources relatively northeast from the antenna at about 10 km, but the field mill still detects a substantial ΔE of −9.4 kV/m. All these flashes lower negative charge from the cloud and produce large ΔE values.

Local meteorological conditions during the lightning episodes were retrieved from the SMC nearby automatic weather station (the AWS is between both towers, 375 m east of the ENT tower) and are summarized in Table 2. Surface negative temperatures and elevated humidity are typical for winter lightning (e.g. Adhikari and Liu, 2019). Besides, strong wind gusts like those recorded on both episodes seem to be necessary to allow upward lightning inception (e.g. Mostajabi et al.,

Table 1

Characteristics of the flashes striking the ENT or the CTA. From the first column: date and time, multiplicity M, average multiplicity $\overline{M}$ for the study area (between brackets) and for the flashes striking ENT or CTA, average peak current $\overline{Ip,\ 1}$ for the strokes of a same flash, average peak current $\overline{Ip,\ 2}$ for the study area and for the day (between brackets) and for all the strokes striking ENT or CTA, inter-stroke time interval, type of the first detection for the flash, electric field jump measured at CS, location of the stroke.

Flashes CG-	Flash multiplicity		Peak current I_p (kA)		Inter-stroke interval (ms)	First detection	ΔE (kV/m)	Location (tower)
Time (UTC)	M	$\overline{M}$	$\overline{Ip,\ 1}$	$\overline{Ip,\ 2}$				
24 March		2.80		−20.3				
20:38:52	3		−15.4		149	CG-	−5.2	CTA
20:39:12	3		−6.0		17	CG-	−0.5	CTA
20:57:01	2		−22.4		55	IC	−6.9	CTA
20:57:52	1		−12.6			IC	−1.9	CTA
20:58:51	1		−22.8			CG-	−5.2	CTA
20:59:25	3		−5.8		18	CG-	−0.85	CTA
20:59:45	11		−6.1		40	CG-	−2.3	CTA
21:02:16	9		−7.9		25	CG-	−5.5	CTA
21:04:31	4	3.67	−17.5	−10.6	25	IC	−12.0	ENT
21:05:26	1		−4.1			CG-	−1.4	ENT
21:07:34	1		−16.7			CG-	−5.4	ENT
21:10:04	8		−9.8		63	CG-	−5.2	CTA
21:14:06	1		−15.3			IC	−11.9	CTA
21:14:54	7		−11.2		27	IC	−4.5	CTA
21:16:42	4		−9.3		38	CG-	−8.2	CTA
21:20:17	3		−11.9		30	CG-	−9.2	ENT
22:00:24	3		−19.7		18	IC	−7.0	CTA
22:14:25	1		−7.5			IC	−2.6	CTA
31 March		1.70		−12.6				
18:44:20	3	3	−12.9	−11.9	201	IC	−11.8	ENT
18:48:49	3		−10.9		187	CG-	−9.4	CTA

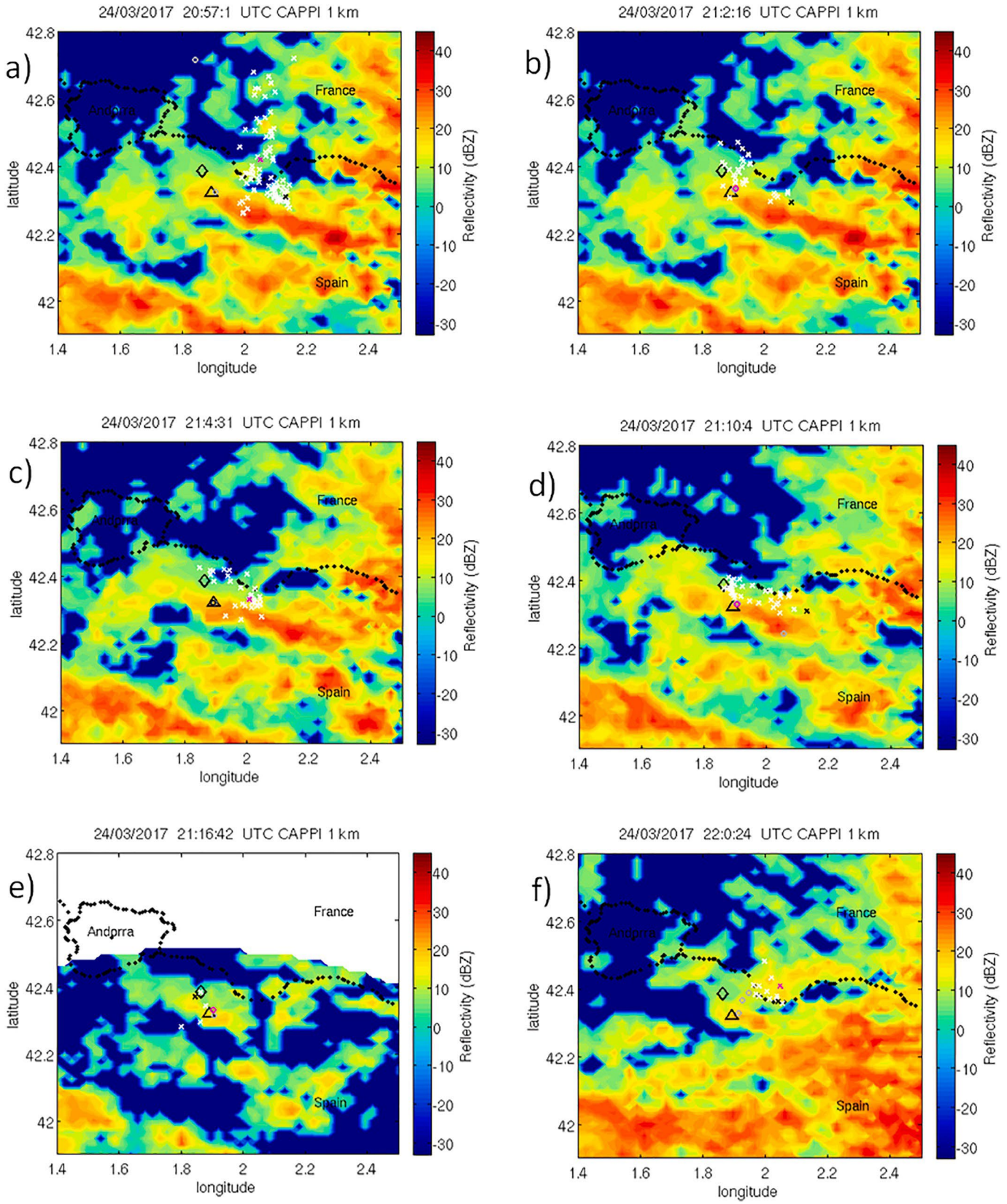

Fig. 7. Reconstruction of six individual CG- flashes from March 24 (a-f), superimposed on CAPPI of radar reflectivity. The VHF sources are indicated by crosses (magenta, white and black if they are the first, intermediate and last detection of the flash, respectively) and the CG- strokes by circles (magenta, grey and black if they are the first, intermediate or last detection of the flash, respectively). The black triangle and diamond indicate the location of the ENT and the CS.

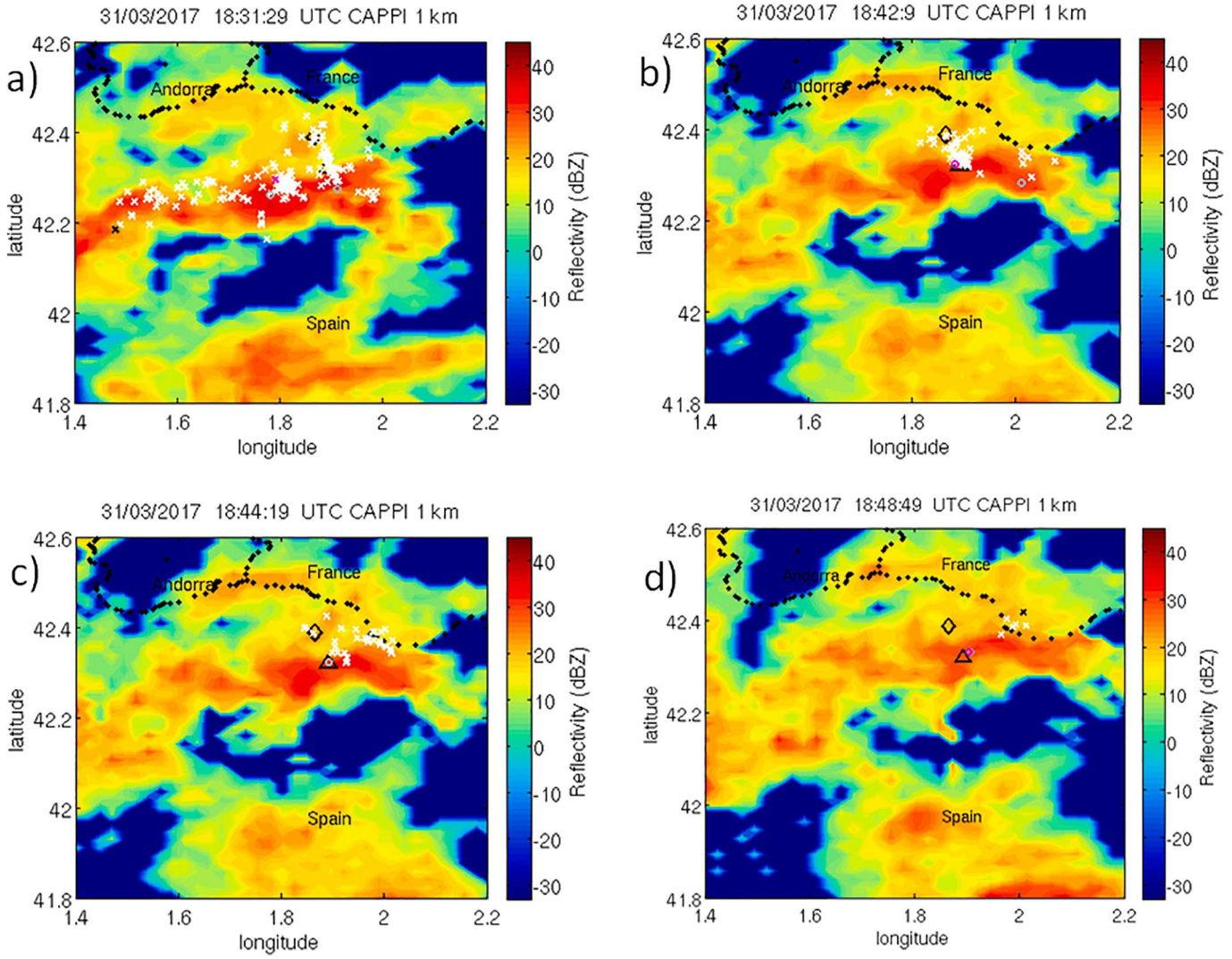

Fig. 8. Same as Fig. 7 for four CG- flashes from March 31 (a–d).

2018), since strong winds (above 8–12 m s^{-1}) remove the corona shield, clearing the way for the upward leader inception (Mazur, 2016).

4. Discussion

4.1. Flash characteristics

The storm activity from two days during Cerdanya-2017 field campaign is analyzed in terms of cloud structure, lightning flash characteristics and surface electric field in the area surrounding ENT and at the ground measurement site in Cerdanya aerodrome. This activity is very different in many ways, especially in the number of lightning strikes on high structures located in the vicinity of Tosa d'Alp (ENT and CTA). Indeed, on March 24 the site of this tower was struck by 18 flashes during a couple of hours of electrical activity detected by Météorage, XDDE and the CS field mill, 8 km away. On the contrary, it was struck by only two flashes on March 31. Furthermore, the difference is even larger for the number of strokes, with 66 for March 24 and only 6 for March 31, which means an average multiplicity of 3.67 and 3, respectively. The comparison with the CG flashes in the region on both days shows the multiplicity is substantially larger for the flashes that strike ENT and CTA. On the contrary, the peak current is much lower for these strokes on March 24 (−10.6 kA for the strokes on ENT and CTA and — 20.3 kA for the strokes over the whole day). On March 24, all the 18 flashes with VHF sources detected at a distance lower than 5 km strike ENT or CTA while on March 31 only 2 out of 8 flashes strike it. The detailed analysis of the stroke location on the site shows that a large majority of flashes (14 over 18) strike CTA on March 24, and the difference is even larger when considering the strokes (57 over 66) since the flashes with the stronger multiplicity strike CTA. It means

Table 2
Temperature, Relative Humidity and Wind conditions at the towers during both periods of lightning activity.

		Temperature (°C)		Relative humidity (%)	Wind speed (m s^{-1})	
Date	Period	Average	Minimum (time)	Range	Average	Max. gust (time)
2017-03-24	20:30–22:30	−1.7	−2.1 (22:29)	100	17.3	33.1 (21:44)
2017-03-31	18:00–19:30	−1.3	−1.5 (19:29)	100	7.1	17.5 (18:55)

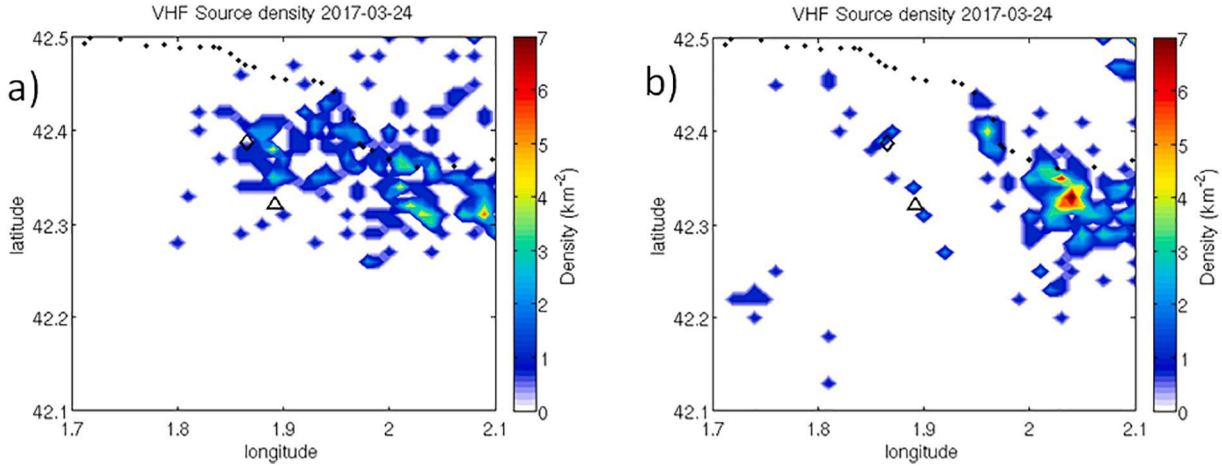

Fig. 9. Density of VHF sources detected by the XDDE in a 0.4° × 0.4° area around the ENT on March 24: a) for the flashes striking the ENT or the CTA and b) for all the other flashes that did not strike it (4 CG- flashes and 1 IC flash).

the average multiplicity is about 4 for the flashes striking CTA and only 2.25 for those striking ENT. The CTA seems to have more ability to be struck by flashes on that day with comparable conditions since the distance is 1.3 km and even its altitude is little lower by 220 m compared to ENT (2315 m against 2537 m). However, the height of ENT is only 25 m and that of CTA is 31 m. It confirms that the height of the tall structure has a bearing on the flash characteristics estimated by the LLS (e.g. Bermudez et al., 2007; Pavanello et al., 2007; Diendorfer et al., 2009).

Thus, all characteristics observed on March 24 (negative polarity, low average peak current, high multiplicity and short interstroke interval) provide evidence regarding the upward nature of the lightning reported on this episode. Indeed, the negative polarity is a characteristic generally observed for the upward lightning initiated from tall structures according to several studies. Diendorfer et al. (2011) found 94% of the 651 lightning flashes striking the Gaisberg tower in Austria lowered negative charge from the cloud while only 4% lowered positive charge and the others were bipolar. Another study by Wang and Takagi (2012) with 100 upward flashes analyzed, concluded that 67.6% of the cases exhibited negative polarity, and 26.5% presented bipolar currents. Jiang et al. (2014) analyzed 8 upward flashes that struck a 325-m tower in Beijing and all were negative. Other studies showed that a tall tower increases the density of negative strokes, especially in the cold season (Kingfield et al., 2017; Zhang et al., 2017). For flashes striking wind turbines, the same characteristic of dominant negative polarity is observed (Pineda et al., 2018a; Soula et al., 2019). For the multiplicity, the result is also relevant since according to several studies, it is larger for the upward lightning flash than for downward flashes (Schultz et al., 2018; Pineda et al., 2019). Regarding the inter-stroke interval, figures on March 24 (40 ms in average) are similar to those reported in other towers. Diendorfer et al. (2009) reported an average interstroke interval of 17.3 ms (median 18.6 ms) at the Gaisberg tower, significantly shorter than observed in triggered and natural downward lightning. A similar result was found at Säntis tower (17.2 ms, Romero et al., 2013), when the average for Switzerland is of 60 ms (Manoochehrnia et al., 2007).

The fact that upward flashes can be initiated by tall structures raises another question about the conditions of triggering. Initially, it was considered that the high electric field for upward leader initiation was produced by in-cloud discharge (Berger and Vogelsanger, 1969). This assumption was not confirmed by Takagi et al. (2006) with simultaneous measurements of *E*-fields and high-speed images during winter storms at Hokuriku areas of Japan: from observation of nine upward positive leaders on high grounded-structures, they found none of which were initiated with apparent in-cloud discharge activity around. A classification of upward flashes was proposed by Wang et al. (2008) as "other-triggered" if they were triggered by prior lightning flash near the tall structure and "self-triggered" if not. Wang et al. (2008) showed that out of 14 upward leaders analyzed, 10 were initiated by nearby lightning discharges while the other 4 were apparently initiated without any preceding discharges. On the contrary, Zhou et al. (2012) studied 205 samples of upward lightning at the Gaisberg Tower during 2005–2009 and found 87% belonged to the "self-triggered" type. Another result by Wang and Takagi (2012) showed the question is complex and probably involves several parameters since they noted that self-triggering occurred more frequently with higher observed wind speeds. We can also cite Warner et al. (2012) who analyzed upward lightning flashes from 10 towers at Rapid City in South Dakota, USA, and found that most of the upward lightning involved preceding flash activity, especially the +CG stroke. In the present study, we have a sample of 20 flashes that strike a tall structure on a mountain peak. The information available from two lightning detection systems allows us to say that 12 flashes start with a detection classified as CG- stroke located at one of both high structures and 8 flashes start with a VHF source detected within the cloud system. For the 12 cases that start with a CG- stroke, the probability is of course high for them to be self-triggered lightning.

In order to better characterize the flashes that strike a high structure on March 24, we consider the flashes with VHF sources detected within a circle at 20 km around ENT. Only 5 flashes do not strike ENT or CTA, while 18 flashes strike it. Among the five flashes that do not strike it, four are CG flashes and one is IC flash. Fig. 9a displays the density of VHF sources detected by the XDDE for the flashes that strike ENT or CTA and Fig. 9b displays it for the flashes that do not strike it, in a 0.4° × 0.4° area. Despite the fact that the number of flashes is much larger in Fig. 9a, the VHF source density is lower with a local maximum at 5.5 km^{-2} and far from ENT (~20 km). In Fig. 9b it is more con- centrated with larger values in the eastern part of the area with a maximum value of 7 km^{-2}. Around ENT the VHF density displays some scattered spots of about 4 strokes per km^2 especially in Fig. 9a, and very small values in Fig. 9b that could be due to "isolated" VHF sources. It means that all flashes detected close to the tower and the antenna strike them on that day and furthermore they radiate little in VHF compared to other flashes detected further. They are different in density of ne- gative leaders that radiate much in VHF, which suggests that a good proportion of these flashes are self-initiated on one of the structures.

4.2. *Meteorological conditions*

Meteorological conditions of both days have been examined using meteorological analysis charts and soundings made at CS on both days

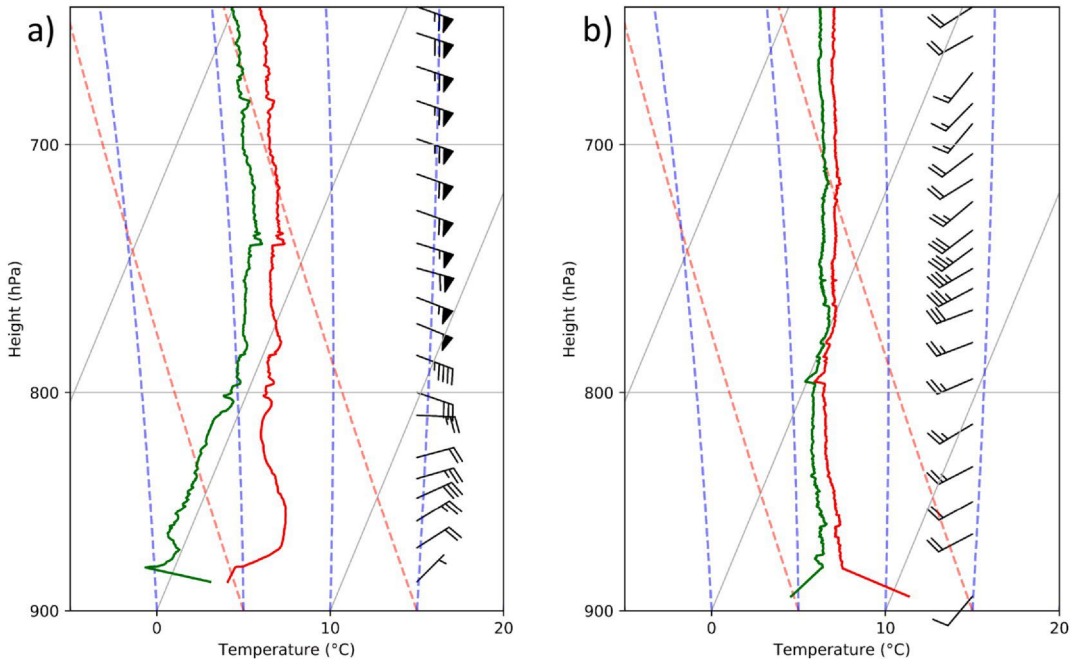

Fig. 10. Atmospheric sounding at CS on 24 March at 22:34 UTC (a) and 31 March at 19:11 UTC (b).

(Fig. 10). On March 24, a deep cyclonic vortex located over France and Spain and cold mid-level air mass within that vortex created the instability favorable for thunderstorms development. Indeed, temperatures below −30 °C and strong southerly air flow at about 5500 m of altitude at the beginning of the day (00:00 UTC) were estimated by forecasting, above the region of the experiment Cerdanya-2017. The sounding made at CS at the end of the day (22:30 UTC) on that day shows −25 °C at 6000 m. At low levels, a surface depression located in the western Mediterranean organized the warm and cold air masses and the surface flows. Several ingredients as the surface low of pressure, a low-level frontal jet, moist air at low level with mixing ratios around 9 g/kg result in 500–1000 J/kg MLCAPE favoured the substantial risk for excessive rain. Precipitation levels exceeded 100 mm locally and about 430 lightning flashes were recorded in a large area for that day in Catalonia.

On March 31, a large long-wave trough oriented north-south west of the coasts of Europe travels slowly eastwards and creates favorable conditions for deep moist convection on its eastern flank over Spain. Indeed, source of convection is available thanks to westerly cold air mass overlapping with southerly warm air carrying large mixing ratios producing CAPE up to around 1000 J/kg. Cumulative rainfall on that day reaches 50 mm very locally in the region of the experiment, when thundercells develop and move northeastwards. The number of flashes detected in the same reference area as for March 24 reaches 745 on that day.

There is an apparent paradox to have much more flashes striking ENT or CTA on March 24 since many parameters seem to characterize less strong convective and lightning activities in the study area. The changes in the vertical profiles of MRR reflectivity and Doppler velocity indicate transitions among different precipitation types, complementing information from operational weather radars. One of the more significant features of the MRR, given its relatively good vertical resolution compared to standard scanning weather radars, is the ability to detect the melting layer. This feature appears as a layer of high reflectivity owing to ice becoming water-coated during the melting phase and a sharp increase of fall speed of precipitation particles (Yuter and Houze Jr., 2003; Smith and Blaes, 2015; Massmann et al., 2017). In the present study, Fig. 4 clearly depicts a melting layer around 1000 m agl (2100 m asl). Although less clear, Fig. 2 also shows a transition at a similar height. Therefore, lightning activity at ENT and CTA, and surroundings during both episodes occur under snowing conditions, and can be considered winter-type lightning. However, the main difference between both days concerns the radar spectral widths and temperature profiles. The radar spectral width in the first case study is substantially higher than in the second. In both cases, spectral width increases coincide with the local electrical field oscillation at ground level at CS. When spectral width exceeds 1.5 m s^{-1} (20:30–21:30 UTC, 24 March) electrical field oscillations present a maximum and also there is lightning activity at ENT; when spectral width ranges between 0.5 and 1.5 m s^{-1} then there are also electrical field oscillations as lightning is more distant; and, finally, when spectral widths are lower than 0.5 m s^{-1} (19:15–20:15 UTC, 31 March) electrical field oscillations are minimal or non-existent. The microphysical process behind this behaviour is likely related to increased accretion and riming suggested by high spectral width values linked to the presence of graupel (Colle et al., 2014).

Regarding the temperature profiles, the 0° isotherm deduced from radiometer data is at about 600 m agl at the beginning of the storm activity, then goes up to 1000 m agl during the storm on March 24, while these heights are around 1300 m agl on March 31. The CTT above the site reaches −55 °C at about 8000 m high on March 24 and −60 °C at more than 10,000 m high on March 31. That means the cloud ne- gative charge generated at temperatures ranging around −15 °C is much closer to the ground on March 24. Indeed, according to the sounding on March 24, the isotherm −15 °C should be at about 3500 m agl which is about 1000 m above the tower location. This proximity can produce large values of the electric field on both tower and antenna to trigger upward leaders, positive in this case toward the negative charge of the cloud. Since positive leaders do not radiate much in VHF (Rakov and Uman, 2003), very few sources are detected by the XDDE. Indeed, our conceptual model on the meteorological conditions favoring winter-type lightning at the ENT is as follows:

(i) On the basis of the non-inductive charging mechanism, the appearance of radar echoes greater than 30–35 dBZ above the −10 °C isotherm is indicative of a substantial amount of hydrometeor particles in the mixed phase region for electrical charging (Takahashi, 1978; Saunders et al., 2006).

(ii) Shindo et al. (2015) observed that upward lightning at the Tokyo Skytree tended to occur when the altitude of −10 °C is below 6 km. Similar observations have been reported in other instrumented towers like Peissenberg, Germany (Heidler et al., 2013), Gaisberg, Austria (Zhou et al., 2014), Morro do Cachimbo, Brazil (Araujo et al., 2012), and also at Säntis in Switzerland (Azadifar et al., 2016; Pineda et al., 2019). Regarding the ENT, previous studies (Montanyà et al., 2012; Pineda et al., 2018a) also reported upward activity when the −10 °C isotherm is low.

(iii) The height of −10 °C temperature level relates to the lower part of the main negative charge layer at moderate convection (Krehbiel, 1986; Stolzenburg et al., 1998). This relationship is valid under different climatic regions, different types of storms and across the seasons (e.g. Shindo et al., 2015; Salvador et al., 2020). Thus, these environmental temperatures also apply to winter storms.

(iv) In term of electrification, the bright band signature is indicative of a change in the dielectric constant. Balloon-borne observations reported a dense charge layer near the 0 °C isotherm (e.g. Sheperd et al., 1996; Rust and Trapp, 2002; Stolzenburg et al., 2007). Sheperd et al. (1996) and others (Stolzenburg and Marshall, 2008 and references therein) have associated the layers of charge near the 0 °C level with the melting process, as evidenced by the presence of a radar bright band. AWS measurements (Table 2) confirm, with negative temperatures, that both ENT and CTA towers were above the melting level during lightning.

When these conditions are met, like in the present case studies, the tip of ENT is beyond the maximum potential associated with the lower charge layer (melting level), exposing the tip of the tower to the main negative charge layer, thus setting favorable conditions for the inception of upward lightning. Although there were no measurement allowing inferring the polarity of the upward leaders, the negative polarity of the recorded return strokes indicates upward leaders were positive, at least on March 24. If the opposite is the case, where the tower would have been exposed to a main positive charge layer instead, the upward leaders emerging from the tower would have been of ne- gative polarity (and the return strokes positive). Eventually, the in- ception of negative upward lightning is more difficult, as more intense electric fields are required, by a factor of about two (Bazelyan et al., 2015).

In addition to the meteorological aspects that set a favorable environment for winter lightning, local wind conditions around the tower tip may play role in the upward leader inception (Table 2). It appears that a strong wind would be necessary to remove the corona shield at the tower tip, clearing the way for the inception of an upward leader (Wang and Takagi, 2012; Warner et al., 2014). According to Mazur (2016) this is the most probable explanation for self-initiated upward lightning in the absence of nearby preceding lightning activity. Warner et al. (2014) suggested a wind speed threshold of 8 m s^{-1}. Mostajabi et al. (2018) analyzed the influence of the wind speed on a long dataset of upward lightning at Säntis tower. They found that above 12 m s^{-1}, almost only self-initiated lightning occurs at Säntis. In the present case study, strong wind gusts (> 30 m s^{-1} and > 15 m s^{-1}) were recorded by the AWS in the vicinity of the tower, for March 24 and 31, respec- tively. The soundings made at CS on both days and plotted in Fig. 10 confirm the presence of stronger winds at the altitude of Tosa d'Alp.

5. Conclusion

We analyze lightning data and thundercloud characteristics recorded on two days of March 2017 during Cerdanya-2017 campaign thanks to remote sensing products and local measurements performed at Cerdanya Station. These two storm days exhibit very different numbers of flashes striking high structures on Tosa d'Alp more than 2500 m high and 8 km from CS. One structure is an instrumented tower 25 m high (ENT) and another is a communication antenna 31 m high (CTA). On March 24, we count 18 flashes including 66 strokes located on this mountain during the storm activity and on March 31, only 2 flashes including 6 strokes. The main observations are summarized in the following. (i) Two structures are struck by these flashes, ENT and CTA separated by 1.3 km. A large majority of the flashes are detected on CTA that is at a lower altitude but a little taller with 31 m compared to 25 m. Thus, during a winter storm, a tall structure on a mountain top can be struck by a great number of flashes, up to 14 flashes in less than two hours for an antenna. (ii) A high proportion of the flashes that strike a tall structure exhibit the characteristics of upward flashes: ne- gative polarity, large multiplicity, low peak current and short inter- stroke time. They produce a negative variation of the electrostatic field measured at CS, which confirms the negative polarity and a substantial charge amount neutralized within the cloud. (iii) A high proportion of these flashes have a CG- stroke as first detection with little VHF ra- diations at the neighboring of the structure. They are good candidates to be considered as self-triggered flashes. (iv) On March 24, all the 18 flashes with VHF sources detected in a radius of 5 km around the structures strike one of them. On March 31, only two flashes out of seven that produce VHF sources in the same area, strike one of the towers. The conditions for striking the towers are much better on March 24, although all observations show stronger convective activity and more CG flashes in the study area on March 31. (v) A common condi- tion on both days that can explain the ability to strike the towers is the altitude of the cloud region with a temperature around −15 °C which is the prime area for non-inducting charging process. (vi) Although both days show convective activity, meteorological features that seems to make a difference are the higher Doppler spectral width on 24 March, as well as the stronger wind at low levels on this day, which removes the corona shield at the tower tip, clearing the way for the inception of upward lightning.

Declaration of Competing Interest

The authors declare that they have no known competing financial interests or personal relationships that could have appeared to influence the work reported in this paper.

Acknowledgments

The Cerdanya-2017 field campaign was a research effort organized by the University of the Balearic Islands, the University of Barcelona, METEO-FRANCE and the Meteorological Service of Catalonia. It was funded by the projects CGL2015-65627-C3-1-R, CGL2015-65627-C3-2- R (MINECO/FEDER), CGL2016-81828-REDT and RTI2018-098693-B- C32 (AEI/FEDER). We thank METEO-FRANCE/CNRM/GMEI/LISA, 4 M and TRAMM teams for the data acquisition during the campaign, especially Jean-Marie Donier and Alexandre Paci from CNRM. Precipitation and microphysics studies of the campaign were performed under the framework of the HyMeX (HYdrological cycle in the Mediterranean EXperiment) international program. The contribution of the Universitat Politècnica the Catalunya was funded by the Spanish Ministry of Economy and the European Regional Development Fund (FEDER): ESP2015-69909-C5-5-R, ESP2017-86263-C4-2-R and ENE2017-91636-EXP. We thank the French Météorage group for providing data on lightning detections.

References

Adhikari, A., Liu, C., 2019. Geographical distribution of thundersnow events and their properties from GPM Ku-band radar. J. Geophys. Res. Atmos. 124, 2031–2048. https://doi.org/10.1029/2018JD028839.

Adirosi, E., Baldini, L., Roberto, N., Gatlin, P., Tokay, A., 2016. Improvement of vertical profiles of raindrop size distribution from micro rain radar using 2D video disdrometer measurements. Atmos. Res. 169, 404–415.

Araujo L.S., Guimaraes, M.B., Pedrosa, A.G., Murta Vale, M.H., Visacro, S., 2012. Assessing events of upward lightning measured at Morro do Cachimbo Station. In:

31st International Conference on Lightning Protection (ICLP) Vienna, pp. 1–4. https://doi.org/10.1109/ICLP.2012.6344331.
Argemí, O., Altube, P., Rigo, T., Ortiga, X., Pineda, N., Bech, J., 2014. Towards the improvement of monitoring and data quality assessment in the weather radar network of the Meteorological Service of Catalonia. In: 8th European Conference on Radar in Meteorology and Hydrology (ERAD). Garmisch-Partenkirchen, Germany (Sept. 2014).
Azadifar, M., Rachidi, F., Rubinstein, M., Paolone, M., Diendorfer, G., Pichler, H., Schulz, W., Pavanello, D., Romero, C., 2016. Evaluation of the performance characteristics of the European Lightning Detection Network EUCLID in the Alps region for upward negative flashes using direct measurements at the instrumented Säntis Tower. J. Geophys. Res. Atmos. 121, 595–606. https://doi.org/10.1002/2015JD024259.
Bazelyan, E.M., Raizer, Yu.P., Aleksandrov, N.L., 2015. The effect of space charge produced by corona at ground level on lightning attachment to high objects. Atmos. Res. 153, 74–86. https://doi.org/10.1016/j.atmosres.2014.07.018.
Becerra, M., Cooray, V., Soula, S., Chauzy, S., 2007. Effect of the space charge layer created by corona at ground level on the inception of upward lightning leaders from tall towers. J. Geophys. Res. 112, D12205. https://doi.org/10.1029/2006JD008308.
Bech, J., Codina, B., Lorente, J., Bebbington, D., 2003. The sensitivity of single polarization weather radar beam blockage correction to variability in the vertical refractivity gradient. J. Atmos. Ocean. Technol. 20 (6), 845–855.
Bech, J., Pineda, N., Rigo, T., Aran, M., 2013. Remote sensing analysis of a mediterranean thundersnow and low-altitude heavy snowfall event. Atmos. Res. 123, 305–322. https://doi.org/10.1016/j.atmosres.2012.06.021.
Bendix, J., Rollenbeck, R., Reudenbach, C., 2006. Diurnal patterns of rainfall in a tropical Andean valley of southern Ecuador as seen by a vertically pointing K-band Doppler radar. Int. J. Climatol. 26, 829–846.
Berger, K., Vogelsanger, E., 1969. New results of lightning observations. In: Coroniti, S.C., Hughes, J. (Eds.), Planetary Electrodynamics. Gordon and Breach, New York, pp. 489–510.
Bermudez, J.L., Rachidi, F., Janischewskyj, W., Shostak, V., Rubinstein, M., Pavanello, D., Hussein, A.M., Chang, J.S., Paolone, M., 2007. Determination of lightning currents from far electromagnetic fields: effect of a strike object. J. Electrost. 65, 289–295. https://doi.org/10.1016/j.elstat.2006.09.007.
Colle, B.A., Stark, D., Yuter, S.E., 2014. Surface microphysical observations within East coast winter storms on long Island, NewYork. Mon. Weather Rev. 142, 3126–3146.
Conangla, L., Cuxart, J., Jiménez, M.A., Martínez-Villagrasa, D., Miró, J.R., Tabarelli, D., Zardi, D., 2018. Cold-air pool evolution in a wide Pyrenean valley. Int. J. Climatol. 38 (6), 2852–2865.
Cummins, K.L., Murphy, M.J., 2009. An overview of lightning location systems: history, techniques, and data uses with an in-depth look at the U.S. NLDN. IEEE Trans. Electromagn. Compat. 51, 499–518.
Diendorfer, G., Pichler, H., Mair, M., 2009, Aug. 2009. Some parameters of negative upward-initiated lightning to the Gaisberg tower (2000–2007). IEEE Trans. Electromagn. Compat. 51 (3), 443–452.
Diendorfer, G., Zhou, H., Pichler, H., Thottappillil, R., 2011. Review of upward positive and bipolar lightning flashes at the Gaisberg Tower. In: Paper Presented at 7th Asia-Pacific International Conference on Lightning, pp. 263–267 Chengdu.
Garrett, T.J., Yuter, S.E., Fallgatter, C., Shkurko, K., Rhodes, S.R., Endries, J.L., 2015. Orientations and aspect ratios of falling snow. Geophys. Res. Lett. 42, 4617–4622.
Gonzalez, S., Bech, J., Udina, M., Codina, B., Paci, A., Trapero, L., 2019. Decoupling between precipitation processes and mountain wave induced circulations observed with a vertically pointing K-band doppler radar. Remote Sens. 11 (9), 1034.
Heidler, F.H., Manhardt, M., Stimper, K., 2013. The slow-varying electric field of negative upward lightning initiated by the Peissenberg Tower, Germany. IEEE Trans. Electromag. Compat. 55 (2), 353–361.
Jiang, R., Qie, X., Wu, Z., Wanga, D., Liu, M., Lu, G., Liu, D., 2014. Characteristics of upward lightning from a 325-m-tall meteorology tower. Atmos. Res. 149, 111–119. https://doi.org/10.1016/j.atmosres.2014.06.007.
Kingfield, D.M., Calhoun, K.M., de Beurs, K.M., 2017. Antenna structures and cloud-to-ground lightning location: 1995–2015. Geophys. Res. Lett. 44, 5203–5212. https://doi.org/10.1002/2017GL073449.
Kneifel, S., Maahn, M., Peters, G., Simmer, C., 2011. Observation of snowfall with a low-power FM-CW K-bandradar (Micro rain Radar). Meteorog. Atmos. Phys. 113, 75–87.
Knupp, K.R., Coleman, T., Phillips, D., Ware, R., Cimini, D., Vandenberghe, F., Vivekanandan, J., Westwater, E., 2009. Ground-based passive microwave profiling during dynamic weather conditions. J. Atmos. Ocean. Technol. 26 (6), 1057–1073.
Krehbiel, P.R., 1986. The Electrical Structure of Thunderstorms, in the Earth's Electrical Environment. National Academy Press, Washington, DC.
Leung, D.Y.C., Yang, Y., 2012. Wind energy development and its environmental impact: a review. Renew. Sust. Energ. Rev. 16 (1), 1031–1039. https://doi.org/10.1016/j.rser.2011.09.024.
Löhnert, U., Crewell, S., 2003. Accuracy of cloud liquid water path from ground-based microwave radiometry: 1. Dependency on cloud model statistics. Radio Sci. 38 (3), 8041. https://doi.org/10.1029/2002RS002654.
Lojou, J.Y., Murphy, M.J., Holle, R.L., Demetriades, N.W., 2009. Nowcasting of thunderstorms using VHF measurements. In: Betz, H.-D., Schumann, U., Laroche, P. (Eds.), Lightning: Principles, Instruments and Applications. Springer, pp. 253–270.
Maahn, M., Kollias, P., 2012. Improved micro rain Radar snow measurements using Doppler spectra post-processing. Atmos. Meas. Tech. 5 (11), 2661–2673.
Mäkelä, A., Saltikoff, E., Julkunen, J., Juga, I., Gregow, E., Niemelä, S., 2013. Cold-season thunderstorms in Finland and their effect on aviation safety. Bull. Am. Meteorol. Soc. 94, 847–858.
Manoochehrnia, P., Schulz, W., Rachidi, F., Rubinstein, M., 2007. Lightning statistics in the regions of Saentis and St.chrischona towers in Switzerland. 29th International Conference on Lightning Protection Uppsala, Sweden.
Massmann, A.K., Minder, J.R., Garreaud, R.D., Kingsmill, D.E., Valenzuela, R.A., Montecinos, A., Fults, S.L., Snider, J.R., 2017. The Chilean Coastal Orographic precipitation experiment: observing the influence of microphysical rain regimes on coastal orographic precipitation. J. Hydrometeorol. 18 (10), 2723–2743.
Matsui, M., Michishita, K., Yokoyama, S., 2020. Cloud-to-ground lightning flash density and the number of lightning flashes hitting wind turbines in Japan. Electr. Power Syst. Res. 181. https://doi.org/10.1016/j.epsr.2019.106066.
Mazur, V., 2016. Principles of Lightning Physics (IOP Expanding Physics). IOP Publishing, Bristol, UK (ISBN-13: 978-0750311533 ISBN-10:0750311533).
Mendez, Y., Birkl, J., Madsen, S., Montaña, J., 2018. The 2018 revision of the standard IEC 61400–24: lightning protection of wind turbines. In: ICLP-34th International Conference on Lightning Protection 2018. IEEE, pp. 1–6. https://doi.org/10.1109/ICLP.2018.8503411. 2018.
Montanyà, J., Soula, S., Murphy, M., March, V., Aranguren, D., Solà, G., Romero, D., 2009. Estimation of charge neutralized by negative cloud-to-ground flashes in Catalonia thunderstorms. J. Electrost. 67 (2–3), 513–517.
Montanyà, J., van der Velde, O., Williams, E.R., 2014. Lightning discharges produced by wind turbines. J. Geophys. Res. Atmos. 119, 1455–1462. https://doi.org/10.1002/2013JD020225.
Montanyà, J., Fabró, F., van der Velde, O., March, V., Williams, E.R., Pineda, N., Romero, D., Solà, G., Freijo, M., 2016. Global distribution of winter lightning: a threat to wind turbines and aircraft. Nat. Hazards Earth Syst. Sci. 16, 1465–1472.
Mostajabi, A., Sunjerga, A., Azadifar, M., Smorgonskiy, A., Rubinstein, M., Rachidi, F., Diendorfer, G., 2018. On the impact of meteorological conditions on the initiation of upward lightning flashes from tall structures. In: 34th International Conference on Lightning Protection (ICLP), https://doi.org/10.1109/ICLP.2018.8503310.
Pavanello, D., et al., 2007. On return stroke currents and remote electromagnetic fields associated with lightning strikes to tall structures: 2. Experiment and model validation. J. Geophys. Res. 112, D13101. https://doi.org/10.1029/2006JD007959.
Peters, G., Fischer, B., Münster, H., Clemens, M., Wagner, A., 2005. Profiles of raindrop size distributions as retrieved by micro rain radars. J. Appl. Meteorol. 44, 1930–1949.
Peters, G., Fischer, B., Clemens, M., 2010. Rain attenuation of radar echoes considering finite-range resolution and using drop size distributions. J. Atmos. Ocean. Technol. 27, 829–842.
Pineda, N., Montanyà, J., 2009. Lightning detection in Spain: the particular case of Catalonia. In: Betz, H.-D., Schumann, U., Laroche, P. (Eds.), Lightning: Principles, Instruments and Applications. Springer, Netherlands, pp. 161–185.
Pineda, N., Montanyà, J., Salvador, A., Van der Velde, O., López, J., 2018a. Thunderstorm characteristics favouring downward and upward lightning to wind turbines. Atmos. Res. 214. https://doi.org/10.1016/j.atmosres.2018.07.012.
Pineda, N., Bech, J., Montanyà, J., Casellas, E., Romero, D., González, S., 2018b. Meteorological aspects of winter upward lightning from an instrumented tower in the Pyrenees. In: 34th International Conference on Lightning Protection (ICLP), https://doi.org/10.1109/ICLP.2018.8503271.
Pineda, N., Figueras i Ventura, J., Romero, D., Mostajabi, A., Azadifar, M., Sunjerga, A., et al., 2019. Meteorological aspects of self-initiated upward lightning at the Säntis tower (Switzerland). J. Geophys. Res. Atmos. 124 (14), 162–14,183. https://doi.org/10.1029/2019JD030834.
Poelman, D.R., Schulz, W., Diendorfer, G., Bernardi, M., 2016. The European lightning location system EUCLID – part 2: Observations. Nat. Hazards Earth Syst. Sci. 16, 607–616. https://doi.org/10.5194/nhess-16-607-2016.
Rachidi, F., Rubinstein, M., Montanyà, J., Bermudez, J.L., Rodriguez, R., Solà, G., Korovkin, N., 2008. A review of current issues in lightning protection of new generation wind turbine blades. IEEE Trans. Ind. Electron. 55 (6), 2489–2496. https://doi.org/10.1109/TIE.2007.896443.
Rakov, V.A., Uman, M.A., 2003. Lightning: Physics and Effects. Cambridge University Press, Cambridge.
Rizk, F.A.M., 1994. Modelling of lightning incidence to tall structures, part I & II. IEEE Trans. Power Deliv. 9 (1), 162–193.
Romero, C., Rachidi, F., Paolone, M., Rubinstein, M., 2013, July 2013. Statistical Distributions of Lightning Currents Associated with Upward negative Flashes based on the Data Collected at the Säntis (EMC) Tower in 2010 and 2011. IEEE Trans. Power Deliv. 28 (3), 1804–1812.
Rose, T., Crewell, S., Löhnert, U., Simmer, C., 2005. A network suitable microwave radiometer for operational monitoring of the cloudy atmosphere. Atmos. Res. 75, 183–200. https://doi.org/10.1016/j.atmosres.2004.12.005. Special issue: CLIWA-NET: Observation and Modelling of Liquid Water Clouds.
Rust, W.D., Trapp, R.J., 2002. Initial balloon soundings of the electric field in winter nimbostratus clouds in the USA. Geophys. Res. Lett. 29 (20), 1959. https://doi.org/10.1029/2002GL015278.
Rutledge, S.A., Hobbs, P., 1983. The mesoscale and microscale structure and organization of clouds and precipitation in midlatitude cyclones. VIII: a model for the "seeder-feeder" process in warm-frontal rainbands. J. Atmos. Sci. 40 (5), 1185–1206.
Salvador, A., Pineda, N., Montanyà, J., Solà, G., 2020. Seasonal variations on the conditions required for the lightning production. Atmos. Res., 104981. https://doi.org/10.1016/j.atmosres.2020.104981.
Saunders, C.P.R., Keith, W.D., Mitzeva, R.P., 1991. The effect of liquid water on thunderstorm charging. J. Geophys. Res. 96 (11,007).
Saunders, C.P.R., Bax-Norman, H., Emersic, C., Avila, E.E., Castellano, N.E., 2006. Laboratory studies of the effect of cloud conditions on graupel/crystal charge transfer in thunderstorm electrification. Q. J. R. Meteorol. Soc. 132, 2653–2673. https://doi.org/10.1256/qj.05.218.
Schultz, C.J., Lang, T.J., Bruning, E.C., Calhoun, K.M., Harkema, S., Curtis, N., 2018. Characteristics of lightning within electrified snowfall events using lightning mapping arrays. J. Geophys. Res. Atmos. 123. https://doi.org/10.1002/2017JD027821.
Schulz, W., Diendorfer, G., Pedeboy, S., Poelman, D.R., 2016. The European lightning

location system EUCLID part 1: performance analysis and validation. Nat. Hazards Earth Syst. Sci. 16 (2), 595–605. http://www.nat-hazards-earth-syst-sci.net/16/595/2016/.

Sheperd, T.R., Rust, W.D., Marshall, T.C., 1996. Electric fields and charges near 0°C in stratiform clouds. Mon. Weather Rev. 124, 919–938.

Shindo, T., Miki, T., Saito, M., Asakawa, A., Motoyama, H., Ishii, M., Fujisawa, A., 2015. Meteorological conditions and occurrence of upward lightning at high structures. IEEJ Trans. Power Energy 135 (6), 417–418. https://doi.org/10.1541/ieejpes.135.417.

Smith, B.L., Blaes, J.L., 2015. Examination of a winter storm using a micro rain radar and AMDAR aircraft soundings. J. Oper. Meteor. 3 (14), 156–171. https://doi.org/10.15191/nwajom.2015.0314.

Soula, S., Georgis, J.-F., 2013. Surface electrical field evolution below the stratiform region of MCS storms. Atmos. Res. 132–133, 264–277. https://doi.org/10.1016/j.atmosres.2013.05.008.

Soula, S., Chauzy, S., Chong, M., Coquillat, S., Georgis, J.-F., Seity, Y., Tabary, P., 2003. Surface precipitation current produced by convective rains during MAP. J. Geophys. Res. 108 (D13), 4395. https://doi.org/10.1029/2001JD001588.

Soula, S., Georgis, J.-F., Salaun, D., 2019. Quantifying the effect of wind turbines on lightning location and characteristics. Atmos. Res. 221, 98–110. https://doi.org/10.1016/j.atmosres.2019.01.010.

Souverijns, N., Gossart, A., Lhermitte, S., Gorodetskaya, I.V., Kneifel, S., Maahn, M., Bliven, F.L., van Lipzig, N.P.M., 2017. Estimating radar reflectivity—Snowfall rate relationships and their uncertainties over Antarctica by combining disdrometer and radar observations. Atmos. Res. 196, 211–223.

Stark, D., Colle, B.A., Yuter, S.E., 2013. Observed microphysical evolution for two East Coast winter storms and the associated snow bands. Mon. Weather Rev. 141, 2037–2057.

Stolzenburg, M., Marshall, T.C., 2008. Charge structure and dynamics in thunderstorms. Space Sci. Rev. 137 (1–4), 355–372. https://doi.org/10.1007/s11214-008-9338-z.

Stolzenburg, M., Rust, W.D., Marshall, T.C., 1998. Electrical structure in thunderstorm convective regions: 3. Synthesis. J. Geophys. Res. 103 (D12), 14,097–14,108. https://doi.org/10.1029/97JD03545.

Stolzenburg, M., Marshall, T.C., Rust, W.D., Mareev, E.A., Davydenko, S.S., 2007. The stratiform precipitation region of mesoscale convective systems: inductive charging evidence and global circuit effects. 13th Int. Conf. Atmos. Elec. I, 13–16 (August, Beijing, China).

Takahashi, T., 1978. Riming electrification as a charge generation mechanism in thunderstorms. J. Atmos. Sci. 35, 1536–1548.

Takagi, N., Wang, D., Watanabe, T., 2006. A study of upward positive leaders based on simultaneous observation of E-fields and high-speed images. Trans. Inst. Electr. Eng. Jpn. 126, 256–259.

Trapero, L., Bech, J., Rigo, T., Pineda, N., Forcadell, D., 2009. Uncertainty of precipitation estimates in convective events by the meteorological service of Catalonia radar network. Atmos. Res. 93 (1–3), 408–418.

Trapero, L., Bech, J., Lorente, J., 2013. Numerical modelling of heavy precipitation events over Eastern Pyrenees: analysis of orographic effects. Atmos. Res. 123, 368–383.

Udina, M., Bech, J., Gonzalez, S., Soler, M.R., Paci, A., Ramón Miró, J., Trapero, L., Donier, J.M., Douffet, T., Codina, B., Pineda, N., 2020. Multi-sensor observations of an elevated rotor during a mountain wave event in the Eastern Pyrenees. Atmos. Res. 234, 104698. ISSN 0169-8095. https://doi.org/10.1016/j.atmosres.2019.104698.

Wang, D., Takagi, N., 2012. Characteristics of winter lightning that occurred on a windmill and its lightning protection tower in Japan. IEEJ Trans. Power Energy 132 (6), 568–572. https://doi.org/10.1541/ieejpes.132.568.

Wang, D., Takagi, N., Watanabe, T., Sakurano, H., Hashimoto, M., 2008. Observed characteristics of upward leaders that are initiated from a windmill and its lightning protection tower. Geophys. Res. Lett. 35 (2008), L028031–L028035.

Warner, T.A., Cummins, K.L., Orville, R.E., 2012. Upward lightning observations from towers in rapid city, South Dakota and comparison with National Lightning Detection Network data, 2004–2010. J. Geophys. Res. 117, D19109. https://doi.org/10.1029/2012JD018346.

Warner, T.A., Lang, T.J., Lyons, W.A., 2014. Synoptic scale outbreak of self-initiated upward lightning (SIUL) from tall structures during the central U.S. blizzard of 1–2 February 2011. J. Geophys. Res. Atmos. 119, 9530–9548. https://doi.org/10.1002/2014JD021691.

White, A.B., Gottas, D.J., Strem, E.T., Ralph, F.M., Neiman, P.J., 2002. An automated brightband height detection algorithm for use with Doppler radar spectral moments. J. Atmos. Ocean. Technol. 19, 687–697. https://doi.org/10.1175/1520-0426(2002)019<0687:AABHDA>2.0.CO;2.

Wilkinson, J.M., Wells, H., Field, P.R., Agnew, P., 2013. Investigation and prediction of helicopter-triggered lightning over the North Sea. Met. Apps 20, 94–106.

Yuter, S.E., Houze Jr., R.A., 2003. Microphysical modes of precipitation growth determined by vertically pointing radar in orographic precipitation during MAP. Quart. J. Roy. Meteor. Soc. 129, 455–476.

Zhang, C., Lu, W., Chen, L., Qi, Q., Ma, Y., Yao, W., Zhang, Y., 2017. Influence of the canton tower on the cloud-to-ground lightning in its vicinity. J. Geophys. Res. Atmos. 122, 5943–5954. https://doi.org/10.1002/2016JD026229.

Zhou, H., Theethayi, N., Diendorfer, G., Thottappillil, R., Rakov, V.A., 2010. On estimation of the effective height of towers on mountaintops in lightning incidence studies. J. Electrost. 68, 415–418.

Zhou, H., Diendorfer, G., Thottappillil, R., Pichler, H., Mair, M., 2012. Measured current and close electric field changes associated with the initiation of upward lightning from a tall tower. J. Geophys. Res. 117 (D08102). https://doi.org/10.1029/2011JD017269.

Zhou, H., Diendorfer, G., Thottappillil, R., Pichler, H., Mair, M., 2014. The Influence of meteorological conditions on upward lightning initiation at the Gaisberg Tower. In: International Conference on Lightning Protection (ICLP), pp. 1162–1165. https://doi.org/10.1109/ICLP.2014.6973303.